ESD-TR-77-198

	3
Solid State Research	1977

Lincoln Laboratory

MASSACHUSETTS INSTITUTE OF TECHNOLOGY

LEXINGTON, MASSACHUSETTS

ADA050551

The views and conclusions contained in this document are those of the contractor and should not be interpreted as necessarily representing the official policies, either expressed or implied, of the United States Government.

This technical report has been reviewed and is approved for publication.

FOR THE COMMANDER
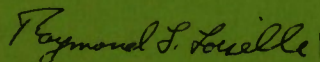
Raymond L. Loiselle

Raymond L. Loiselle, Lt. Col., USAF
Chief, ESD Lincoln Laboratory Project Office

MASSACHUSETTS INSTITUTE OF TECHNOLOGY

LINCOLN LABORATORY

SOLID STATE RESEARCH

QUARTERLY TECHNICAL SUMMARY REPORT

1 MAY – 31 JULY 1977

ISSUED 8 NOVEMBER 1977

Approved for public release; distribution unlimited.

LEXINGTON   MASSACHUSETTS

ABSTRACT

This report covers in detail the solid state research work of the Solid
State Division at Lincoln Laboratory for the period 1 May through
31 July 1977. The topics covered are Solid State Device Research,
Quantum Electronics, Materials Research, Microelectronics, and
Surface-Wave Technology. Funding is primarily provided by the Air
Force, with additional support provided by the Army, ARPA, NSF,
and ERDA.

CONTENTS

INTRODUCTION

I. SOLID STATE DEVICE RESEARCH

The characteristics of CW double-heterostructure GaInAsP diode lasers, which had an emission wavelength of 1.22 μm at 22°C, are reported for heat-sink temperatures up to 50°C. The temperature dependence of the threshold current density for pulsed operation follows the exponential function $J_{th} \propto \exp[T/T_o]$, where $T_o \sim 75°C$.

The previously reported GaAs stepped $\Delta\beta$-reversal electrooptic waveguide switch has been substantially improved. By biasing the electrodes independently, the power isolation at 1.06 μm could be enhanced to 25 dB in each switch state. When considered as a modulator, this device has a calculated power-bandwidth ratio in a 50-Ω system of 40 mW/MHz.

The wavelength dependence of GaAs $p^+n^-n^+$ directional couplers and electrooptic switches has been determined in the range 0.92 to 1.15 μm. It has been found that the coupling length varies faster than inversely with wavelength.

InP has been doped by ion implantation with several ions to yield layers of both n- and p-type conductivity. Se^+ and Si^+ were found to be efficient n-type dopants with activations in excess of 75 percent. Cd^+, Mg^+, and Be^+ were all acceptors, with Mg^+ yielding a sheet hole concentration as high as 5×10^{13} cm^{-2} for a dose of 1×10^{14} cm^{-2} at 150 keV.

II. QUANTUM ELECTRONICS

The characteristics of a passively Q-switched, flash-lamp-excited NdP_5O_{14} laser have been studied as a function of Q-switch dye concentration and output mirror transmission. Up to 2 mJ in a 6-nsec pulse have been obtained with 1-J energy into the lamp.

Using high-optical-quality material grown at Lincoln Laboratory, laser operation at 1.63 μm has been observed in MgF_2:Ni. Lasers of this type, which operate using phonon-assisted electronic transitions, provide a new source of broadly tunable radiation in the near infrared, and may be efficiently optically pumped by a Nd:YAG laser.

An atmospheric pressure mini-TEA CO_2 laser has been designed and constructed. Arc-free pulse energies of 30 mJ and repetition rates over 10 Hz have been obtained with the initial unit.

Studies have been continued on third-harmonic generation (THG) of CO_2 laser radiation in cryogenic liquid CO mixtures. A THG power-conversion efficiency of 2 percent has been obtained using a 100-nsec pump laser pulse length.

Raman scattering measurements of the vibrational frequency and linewidth of liquid CO-O_2, CO-N_2, and CO-Ar mixtures have been carried out. The dipolar broadening due to CO-CO interactions has been shown to dominate the linewidth for high CO concentrations.

Infrared double-resonance measurements have been performed on CO_2 TEA-laser-excited SF_6. A pressure-independent induced-absorption signal, which may be due to a coherent excitation process, is observed. Induced-absorption spectra, obtained as a function time after the excitation pulse, provide information on the flow of energy in the molecule.

III. MATERIALS RESEARCH

A study has been made of the effect of O_2 partial pressure during deposition on the electrical and optical properties of Sn-doped In_2O_3 films obtained by rf sputtering. Close control of the O_2 pressure was found to be essential for the reproducible preparation of high-quality films for use as transparent conductors in optoelectronic devices.

The interaction of H_2O with surfaces of TiO_2 and $SrTiO_3$, two materials that have been successfully used as catalytic electrodes in the photoelectrolysis of H_2O to produce H_2 and O_2, has been investigated by ultraviolet photoemission spectroscopy in ultrahigh vacuum. For low exposures to H_2O vapor, the data for $TiO_2(110)$ surfaces indicate the pressure of OH radicals produced by dissociative chemisorption of H_2O; for $TiO_2(110)$ surfaces at high exposures and for $SrTiO_3(100)$ surfaces at all exposures, the chemisorption of H_2O is nondissociative, but some of the molecular orbitals are shifted in energy with respect to those of the gaseous H_2O molecule.

In a continuing effort to identify new solid electrolytes for use in high-energy-density secondary batteries, it has been found that $Na_5YSi_4O_{12}$ exhibits high Na^+-ion conductivity. For a ceramic rod with 92 percent of theoretical density, the conductivity at 300°C is $\sim 0.1 \ \Omega^{-1} \ cm^{-1}$, compared with $\sim 0.4 \ \Omega^{-1} \ cm^{-1}$ for β-alumina and NASICON.

IV. MICROELECTRONICS

High-efficiency GaAs single-crystal solar cells have been fabricated utilizing a homojunction formed by chemical vapor deposition of a thin n^+ layer on a thicker p layer. Conversion efficiencies of 15.3 percent (17 percent when corrected for contact area) at AM 1 (unity air mass) have been achieved without the use of $Ga_{1-x}Al_xAs$/GaAs heterostructures. These conversion efficiencies are approaching those obtained with heterostructure cells, and are considerably higher than those previously reported for GaAs homojunction devices.

A surface-oriented GaAs Schottky-barrier mixer diode has been used to harmonically mix the 82nd harmonic of an X-band klystron with a 761-GHz submillimeter laser signal. Two methods have been used to couple radiation to the diode. In the first, the surface-oriented diode is connected to a quartz stripline filter structure which is suspended across an overmoded, reduced-height N guide. The second method utilizes integrally connected half-wavelength dipole antennas to enhance the coupling.

A grating mask consisting of 0.635-μm lines and spaces has been fabricated with conventional mask-making apparatus. This resolution (788 line pairs/mm) is 2X greater than the stated optimized specifications for the equipment, and was achieved by precise processing procedures and by a double-reduction technique utilizing 100X reticles and photocomposition of 10X reticles and the final mask. The need for a double-wide space in the center of four of the final gratings represented a major challenge for the pattern generation of the 100X reticle and the photocomposition of the 10X reticle.

V. SURFACE-WAVE TECHNOLOGY

The combination of a new design approach and a simple fabrication procedure has led to the first realization of a practical surface-acoustic-wave two-port resonator with Q at the material limit. In particular, the device on ST quartz exhibited an unloaded Q in excess of 32,000 when operated in vacuum at 310 MHz. The latter value of Q is virtually the same as the best estimate of the material Q at this frequency, which implies that all losses in the system have been rendered negligible in comparison with the intrinsic propagation loss in the material.

A new interferometric alignment technique has been developed that is suitable for aligning x-ray-lithography masks or photomasks relative to a substrate. A superposition precision of 200 Å has been demonstrated and, in principle, better than 100 Å should be possible. The superposition of matching grating-type alignment marks on facing plates is determined from the intensities of beams multiply diffracted from the matching alignment marks.

PUBLISHED REPORTS

Journal Articles

JA No.

4496	Applications of Infrared Lasers to Spectroscopy	A. H. M. Ross[*] P. L. Kelley K. W. Nill[*]	In <u>Frontiers in Laser Spectroscopy</u>, Vol. 2, edited by R. Balian, S. Haroche, and S. Liberman (North-Holland, Amsterdam, 1977), pp. 571-635
4677	Submillimeter Heterodyne Detection with Planar GaAs Schottky-Barrier Diodes	R. A. Murphy C. O. Bozler C. D. Parker H. R. Fetterman P. E. Tannenwald B. J. Clifton J. P. Donnelly W. T. Lindley	IEEE Trans. Microwave Theory Tech. <u>MTT-25</u>, 494 (1977)
4708	Schottky-Barrier Diodes for Submillimeter Heterodyne Detection	B. J. Clifton	IEEE Trans. Microwave Theory Tech. <u>MTT-25</u>, 457 (1977)
4709	Selective Black Absorbers Using rf-Sputtered Cr_2O_3/Cr Cermet Films	J. C. C. Fan S. A. Spura	Appl. Phys. Lett. <u>30</u>, 511 (1977)
4718	Ag_2Se-Ga_2Se_3 Pseudobinary Phase Diagram	J. C. Mikkelsen, Jr.	Mater. Res. Bull. <u>12</u>, 497 (1977)
4721	cw Operation of Distributed Feedback $Pb_{1-x}Sn_xTe$ Lasers	J. N. Walpole A. R. Calawa S. R. Chinn S. H. Groves T. C. Harman	Appl. Phys. Lett. <u>30</u>, 524 (1977)
4722	Polarised Infrared Reflectivity of $CdGeAs_2$	G. D. Holah[*] A. Miller[*] W. D. Dunnett[*] G. W. Iseler	Solid State Commun. <u>23</u>, 75 (1977)
4726	Thin-Film VO_2 Submillimeter-Wave Modulators and Polarizers	J. C. C. Fan H. R. Fetterman F. J. Bachner P. M. Zavracky C. D. Parker	Appl. Phys. Lett. <u>31</u>, 11 (1977)
4728	Flash-Lamp-Excited NdP_5O_{14} Laser	S. R. Chinn W. K. Zwicker[*]	Appl. Phys. Lett. <u>31</u>, 178 (1977)

---

[*] Author not at Lincoln Laboratory.

[*] Author not at Lincoln Laboratory.

*   *   *   *   *

UNPUBLISHED REPORTS

Journal Articles

---

[*] Author not at Lincoln Laboratory.

[*] Author not at Lincoln Laboratory.

[†] Titles of Meeting Speeches are listed for information only. No copies are available for distribution.

---

[*] Author not at Lincoln Laboratory.

4480	Gap-Coupled Schottky-Diode/ LiNbO$_3$ Acoustoelectric Integrating Correlator	R. W. Ralston D. H. Hurlburt F. J. Leonberger J. H. Cafarella E. Stern	35th Device Research Conf., Cornell University, Ithaca, New York, 27-29 June 1977
4523	A Bipolar NPN Transistor with Reduced Low Current β Falloff	G. L. Hansell C. G. Fonstad[*]	
4469	Optically Pumped 16 μm CO$_2$ Laser	R. M. Osgood, Jr.	Lasers for Isotope Separation Conf., Albuquerque, New Mexico, 17-19 May 1977
4502	Lasers at 1.0 - 1.3 μm for Optical Fiber Communications	I. Melngailis	1977 Intl. Conf. on Integrated Optics and Optical Fiber Communications, Tokyo, Japan, 18-20 July 1977
4508	Preparation and Properties of MgO/Au and Cr$_2$O$_3$/Cr Multiphase Films	J. C. C. Fan	New England Symp. of American Vacuum Society, Burlington, Massachusetts, 16 June 1977
4510	Molecular Beam Epitaxial Growth of Thin Semiconductor Films	A. R. Calawa	
4516A	Diode Lasers at 1.0 to 1.3 μm for Optical Fiber Communications	I. Melngailis	NSF Grantee-USER Mtg. on Optical Communications, New York, 6-7 June 1977
4530	IR Spectroscopy via Difference-Frequency Generation	A. S. Pine	3rd Intl. Conf. on Laser Spectroscopy, Jackson, Wyoming, 5-8 July 1977
4535	Advantages and Fabrication of Two-Sided GaAs Power FETs	R. A. Murphy	GaAs FET Applications Workshop, San Diego, 24 June 1977
4537	Vibrational Energy Transfer Processes in Simple Cryogenic Liquids	S. R. J. Brueck R. M. Osgood, Jr. T. F. Deutsch	Gordon Conf. on Molecular Energy Transfer, Wolfeboro, New Hampshire, 11-15 July 1977
4538	Double Resonance Measurements of ν_3 Mode Kinetics of SF$_6$ Under Intense CO$_2$ TEA Laser Excitation	T. F. Deutsch S. R. J. Brueck	
4558	Efficient Infrared Four-Wave Processes in Cryogenic Liquid Mixtures	H. Kildal S. R. J. Brueck	Gordon Res. Conf. on Nonlinear Optics, Plymouth, New Hampshire, 15-19 August 1977

[*] Author not at Lincoln Laboratory.

SOLID STATE DIVISION

A. L. McWhorter, *Head*
I. Melngailis, *Associate Head*
C. R. Grant, *Assistant*

P. E. Tannenwald

QUANTUM ELECTRONICS

A. Mooradian, *Leader*
P. L. Kelley, *Associate Leader*

Barch, W. E.	Hancock, R. C.
Brueck, S. R. J.	Kildal, H.
Burke, J. W.	Menyuk, N.
Chinn, S. R.	Moulton, P. F.
DeFeo, W. E.	Osgood, R. M.
Deutsch, T. F.	Parker, C. D.
Fetterman, H. R.	Pine, A. S.
Fleming, M. W.*	

ELECTRONIC MATERIALS

A. J. Strauss, *Leader*
H. J. Zeiger, *Associate Leader*

Anderson, C. H., Jr.	Kafalas, J. A.
Button, M. J.	Kolesar, D. F.
Chapman, R. L.	Krohn, L., Jr.
Delaney, E. J.	LaFleur, W. J.
Dresselhaus, G.	Mastromattei, E. L.
Dwight, K., Jr.	Mavroides, J. G.
Fahey, R. E.	Mroczkowski, I. H.
Fan, J. C. C.	Owens, E. B.
Feldman, B.	Palm, B. J.
Finn, M. C.	Pantano, J. V.
Gay, R. R.*	Reed, T. G.
Henrich, V. E.	Tchernev, D. I.
Hong, H. Y-P.	Tracy, D. M.
Hsieh, J. J.	Vohl, P.
Iseler, G. W.	

APPLIED PHYSICS

A. G. Foyt, *Leader*
T. C. Harman, *Assistant Leader*
C. E. Hurwitz, *Assistant Leader*

Armiento, C. A.*	Leonberger, F. J.
Belanger, L. J.	Lind, T. A.
Calawa, A. R.	McBride, W. F.
Carter, F. B.	Paladino, A. E.
DeMeo, N. L., Jr.	Plonko, M. C.
Donnelly, J. P.	Shen, C. C.
Ferrante, G. A.	Spears, D. L.
Glasser, L. A.*	Tsang, D. Z.*
Groves, S. H.	Walpole, J. N.

SURFACE WAVE TECHNOLOGY

E. Stern, *Leader*
R. C. Williamson, *Associate Leader*

Baker, R. P.	Kernan, W. C.
Brogan, W. T.	Li, R. C. M.
Cafarella, J. H.	Melngailis, J.
DeGraff, P. D.	Ralston, R. W.
Dolat, V. S.	Reible, S. A.
Efremow, N., Jr.	Schulz, M. B.
Flanders, D. C.	Shaver, D.*
Holtham, J. H.	Smith, H. I.
Hurlburt, D. H.	Vlannes, N.*

MICROELECTRONICS

W. T. Lindley, *Leader*
F. J. Bachner, *Associate Leader*

Beatrice, P. A.	Gray, R. V.
Bozler, C. O.	Hansell, G. L.*
Burke, B. E.	Lincoln, G. A., Jr.
Chiang, A. M.	McGonagle, W. H.
Clifton, B. J.	Mountain, R. W.
Clough, T. F.	Murphy, R. A.
Cohen, R. A.	Pichler, H. H.
Daniels, P. J.	Silversmith, D. J.
Durant, G. L.	Smythe, D. L., Jr.
Foley, G. H.	Wilde, R. E.
Grant, L. L.	

* Research assistant

I. SOLID STATE DEVICE RESEARCH

A. CW OPERATION OF DOUBLE-HETEROSTRUCTURE GaInAsP/InP LASERS UP TO 50°C

We report here CW operation of double-heterostructure (DH) $Ga_x In_{1-x} As_y P_{1-y}$ lasers (x = 0.21, y = 0.50) for heat-sink temperatures up to 50°C. Their emission wavelength at 22°C is 1.22 μm. The temperature dependence of the threshold current density for pulsed operation follows the exponential function $J_{th} \propto exp[T/T_o]$, with $T_o \sim 75°C$.

The DH GaInAsP/InP lasers tested in this work are stripe-geometry devices prepared by the liquid-phase epitaxial technique. They consist of a (111)B-oriented n-type InP substrate (n ~ 4×10^{18} cm^{-3}), an Sn-doped n-InP layer (n ~ 3×10^{18} cm^{-3}), an Sn-doped GaInAsP active layer (n ~ 10^{18} cm^{-3}), and a Zn-doped p-InP layer (p ~ 3×10^{18} cm^{-3}). Both InP layers are 2 μm thick, and the GaInAsP active layer is ~0.2 μm thick. During the growth process, the active layer was converted to p-type by Zn diffusion from the InP capping layer. After growth, samples were processed into proton-defined stripe-geometry lasers. The stripe width is 13 μm, and the cavity length is typically 380 to 400 μm. Ohmic contacts were made by evaporating Au/Zn alloy on the p-side and electroplating Au/Sn on the n-side, then annealing at 380°C in a hydrogen ambient for 10 sec. The total series resistance for these devices is typically 2 to 3 Ω.

In pulsed operation, the diodes were mounted on a testing jig and driven with low duty cycle (100-nsec and 75-pps) pulses. The light output was detected with a Ge avalanche photodiode and displayed on a fast oscilloscope. The lasing spectrum was obtained by focusing the light into a grating spectrometer and detecting the radiation with a cooled S-1 photomultiplier.

A room-temperature threshold current density as low as 4.4 kA/cm^2 was obtained. The total variation in J_{th} for devices fabricated from the same wafer was less than 50 percent. To study the threshold characteristics at different heat-sink temperatures, an individual laser was mounted with p-side down on a diode package using In solder. The diode package was attached to a copper heat sink. The temperature of the heat sink and diode was varied by a thermoelectric cooling and heating device. In Fig. I-1, we plot the pulsed threshold current density vs the heat-sink temperature T for 0°C < T < 50°C. J_{th} was found to increase exponentially with T and can be described by $J = J_o exp[T/T_o]$ with $T_o \sim 75°C$, where J_o is a constant.

In CW operation, each diode was driven with a constant current source. The light output from one facet of the laser was coupled into an optical fiber and detected at the other end with a calibrated Ge photovoltaic cell. In Fig. I-2, the output power was plotted vs operating current for heat-sink temperatures of 22°, 30°, 40°, and 50°C. The differential quantum efficiency is 10 percent per face from 22°C up to 40°C, then drops to 3.6 percent as T is raised to 50°C because of severe joule heating at high operating current. A typical CW emission spectrum at threshold consists of a large number of longitudinal modes which cover a band about 250 to 300 Å wide. The spectrum narrows to only a few longitudinal modes as the pumping current increases to 5 to 10 percent above threshold. In some cases a single mode is exhibited. Figure I-3 shows the emission spectrum for a laser operating at 10 percent above threshold. The temperature dependence of the lasing wavelength λ was investigated by operating the device in the pulsed mode at a controlled heat-sink temperature T. It was found that λ increases linearly with T for 10°C < T < 50°C, with $\Delta\lambda/\Delta T \sim 3.2$ Å/°C.

C. C. Shen
J. J. Hsieh
T. A. Lind
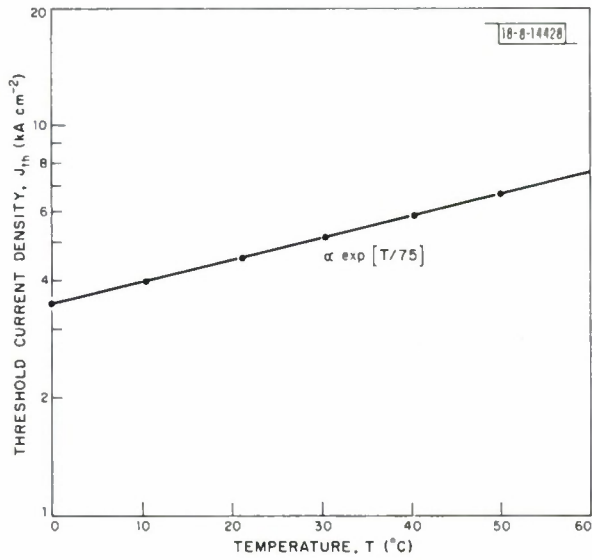
Fig. I-1. Threshold current density vs heat-sink temperature for DH GaInAsP/InP laser emitting at 1.22 μm.
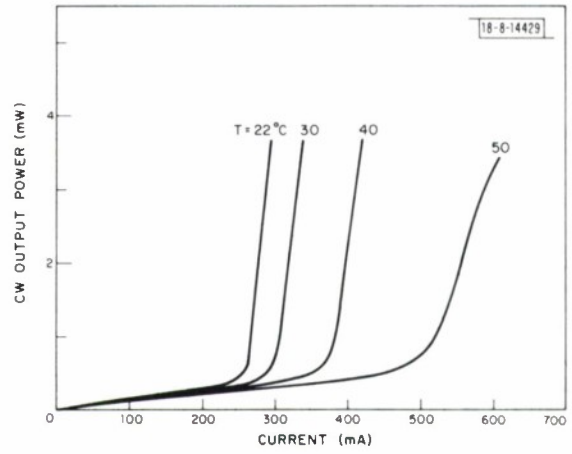
Fig. I-2. CW output power per face vs operating current at different heat-sink temperatures for DH GaInAsP/InP laser.
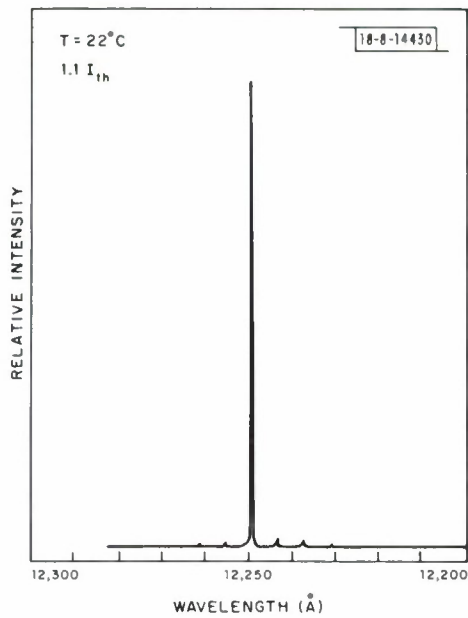
Fig. I-3. CW emission spectrum for DH GaInAsP/InP laser operating at 320 mA (10 percent above threshold). Heat-sink temperature is 22°C.

2

B. GaAs $\Delta\beta$-REVERSAL SWITCH

We have previously reported the first demonstration of a GaAs directional-coupler switch with stepped $\Delta\beta$ reversal.[1,2] For this type of electrooptic 2×2 waveguide switch, both switch states can be electrically optimized so that a high degree of power isolation can be obtained. In Refs. 1 and 2, the fabrication, testing, and operational principles of the device have been discussed. Here, we present data on a $\Delta\beta$-reversal switch fabricated to minimize dimensional asymmetry (i.e., inherent $\Delta\beta$) between the guides. This device has shown more nearly idealized behavior than earlier devices, and has exhibited 23-dB power isolation in both switch states at 1.06 μm with equal bias arrangements of the electrodes (25-dB power isolation in both switch states was achieved with independent biasing of the electrodes). The power-bandwidth ratio of the device as well as its switching characteristics at 1.15 μm will also be reported.

The switch is formed by two metal-clad optical striplines with 8-μm-wide guides having a 4-μm spacing. The device consists of Pt-Au Schottky-barrier electrodes electroplated on a 2.1-μm-thick n$^-$ (6×10^{14} cm^{-3}) epitaxial layer, an n$^+$ (1×10^{18} cm^{-3}) substrate, and an AuSn back contact. The Schottky-barrier electrodes had a 25-μm gap midway along the sample length so that the device actually had six equal-length electrodes. The device length, 10 mm, was ~20 percent greater than the 1.06-μm coupling length.

The switching performance of the device is shown in Fig. I-4(a) for a uniform-$\Delta\beta$ bias arrangement, and in Fig. I-4(b) for a reversed-$\Delta\beta$ bias arrangement. The figures indicate the variation with bias V_s of the output power P_i from the input guide and P_c from the coupled guide, as well as the total output power $P_i + P_c$. The data were obtained by biasing the electrodes equally, as shown in the diagram in the upper right portion of each figure. The measured total power at $V_s = 0$ is the same for both cases. A maximum power isolation of 23 dB is obtained for each bias arrangement with total output power constant to $\leqslant 0.2$ dB. As shown in Fig. I-4(a), the straight-through state is obtained at $V_s = -19$ V, and as shown in Fig. I-4(b), the crossover state is obtained at $V_s = -22$ V. The slight increase in power with bias for the reversed-$\Delta\beta$ bias case is not fully understood but could be associated with changes in mode confinement. By biasing the electrodes independently, power isolation could be improved to 25 dB in each switch state for a voltage difference of <4 V. When considered as a modulator, this device has a calculated power-bandwidth ratio in a 50-Ω system of 40 mW/MHz.

The $\Delta\beta$-reversal switch should be useful over a range of wavelengths. The same device can be used to switch light of any wavelength for which the coupling length is shorter than the sample length, and for which the device exhibits reasonable transmission. We have demonstrated this concept by using the device for which the 1.06-μm results presented above were obtained to achieve switching at 1.15 μm. Preliminary results indicate 22-dB power isolation in the straight-through state, and 25-dB power isolation in the crossover state. These 1.15-μm measurements were made using a GaInAsP/InP DH laser. The device coupling length at 1.15 μm, 7.2 mm, was about 10 percent less than it was at 1.06 μm.

<div style="text-align: right;">

F. J. Leonberger
C. O. Bozler

</div>

C. WAVELENGTH DEPENDENCE OF GaAs p$^+$n$^-$n$^+$ DIRECTIONAL COUPLERS AND ELECTROOPTIC SWITCHES

We have previously reported the fabrication and testing of GaAs p$^+$n$^-$n$^+$ directional couplers[3] and electrooptic switches.[4,5] Here we describe the dependence of coupler and switch characteristics on wavelengths in the range 0.92 to 1.15 μm. We find that the coupling length
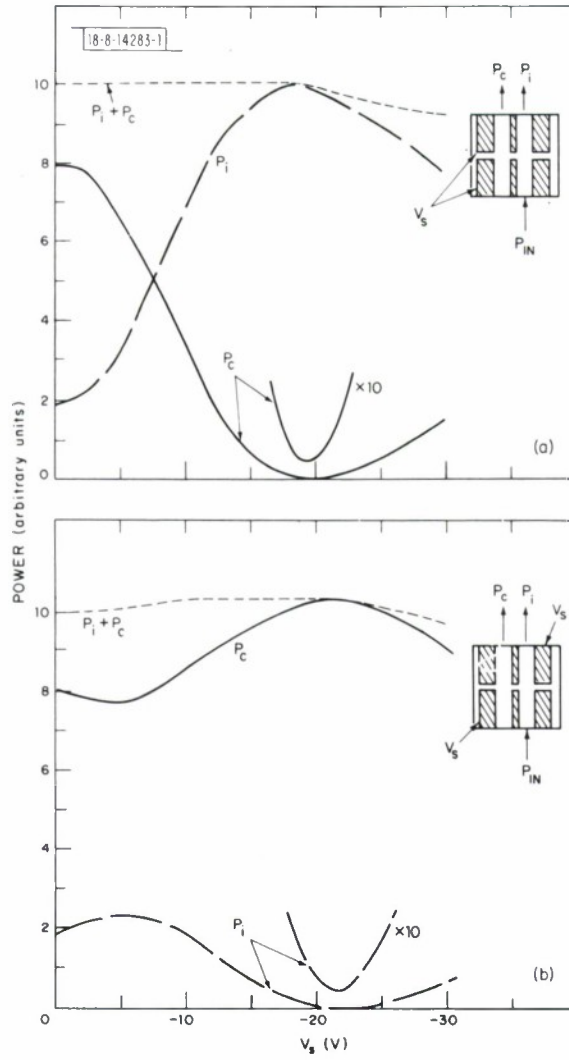
Fig. I-4. Power vs bias for each guide of GaAs switch for (a) uniform-$\Delta\beta$ bias arrangement and (b) reversed-$\Delta\beta$ bias arrangement. A 10X magnified trace is shown for guide in which light is extinguished. Diagram in upper right portion of each figure indicates bias arrangement.

varies faster than inversely with wavelength, especially near 0.92 μm. This effect can be attributed to the variation of the effective guide index with wavelength. Switch performance at 1.06 and 1.15 μm is consistent, while at 0.92 μm there is a decrease in total power output with applied bias that could be attributed to electroabsorption effects.

The devices were fabricated from a closely spaced pair of GaAs $p^+n^-n^+$ channel-stop optical strip waveguides. A schematic cross section of the device structure is shown in Fig. I-5. As described in detail in Ref. 3, the structure consists of three p^+ (3×10^{18} cm^{-3}) regions formed by Be$^+$-ion implantation in an n^- (6×10^{14} cm^{-3}) guiding layer. The substrate is n^+ (1×10^{18} cm^{-3}) and has an AuSn back contact. Microalloyed AuZn electrodes are used to form contacts to the p^+ regions. Light is guided in the two channels between the three p^+ regions because the effective guide index is highest there. The guides reported here are single-mode and are typically 8.5 μm wide with a 4-μm gap. The epitaxial layer and the p^+ regions are ~4.5 and 1.6 μm thick, respectively. With no bias applied to the p^+n^- junctions, the device functions as a passive directional coupler. If the device is a coupling length long, essentially all the light at the output face will be confined to the coupled guide at zero bias and can be switched to the input guide with the appropriate applied voltage.

Measurements of coupling length and switching performance were made at 1.15, 1.06, and 0.92 μm in a manner that has previously been described.[3,4] The 1.15- and 0.92-μm measurements utilized a GaInAsP/InP DH diode laser and a GaAlAs/GaAs DH diode laser, respectively. The 1.06-μm data were obtained using an Nd:YAG laser. In each case, the laser light was TE polarized and end-fire coupled into one of the two guides at the cleaved input face of the device. The near-field intensity pattern of the two guides at the device output face was imaged on an Si diode array vidicon for display on a television monitor and on a slit in front of an Si photodiode for quantitative measurements.

The variation of coupling length L_c with wavelength λ for two devices is shown in Fig. I-6. These devices have the dimensions given above, but similar results were obtained for devices with 6-μm-wide guides and 6-μm spacing and for devices of similar dimensions with epitaxial
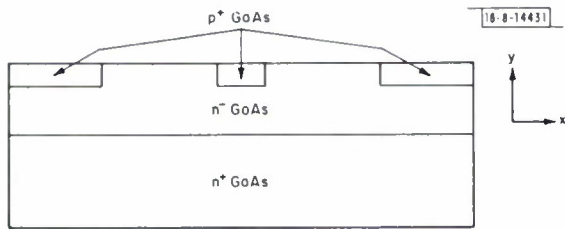
Fig. I-5. Schematic cross section of GaAs $p^+n^-n^+$ directional coupler.
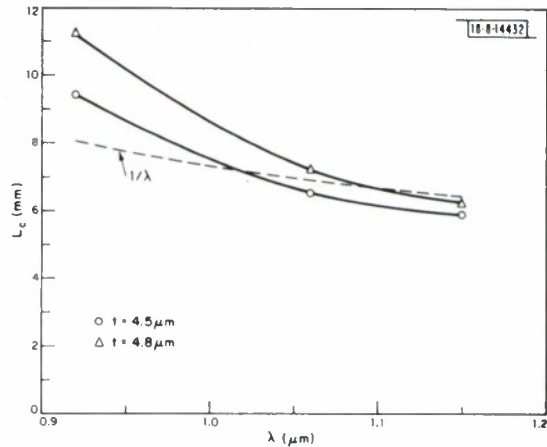
Fig. I-6. Variation of coupling length L_C vs wavelength for two directional couplers having an 8.5-μm guide width, a 4-μm guide spacing, and an epitaxial layer thickness t. Measured values of L_C are accurate to ±5 percent. Dashed curve indicates a $1/\lambda$ dependence of L_C.

5
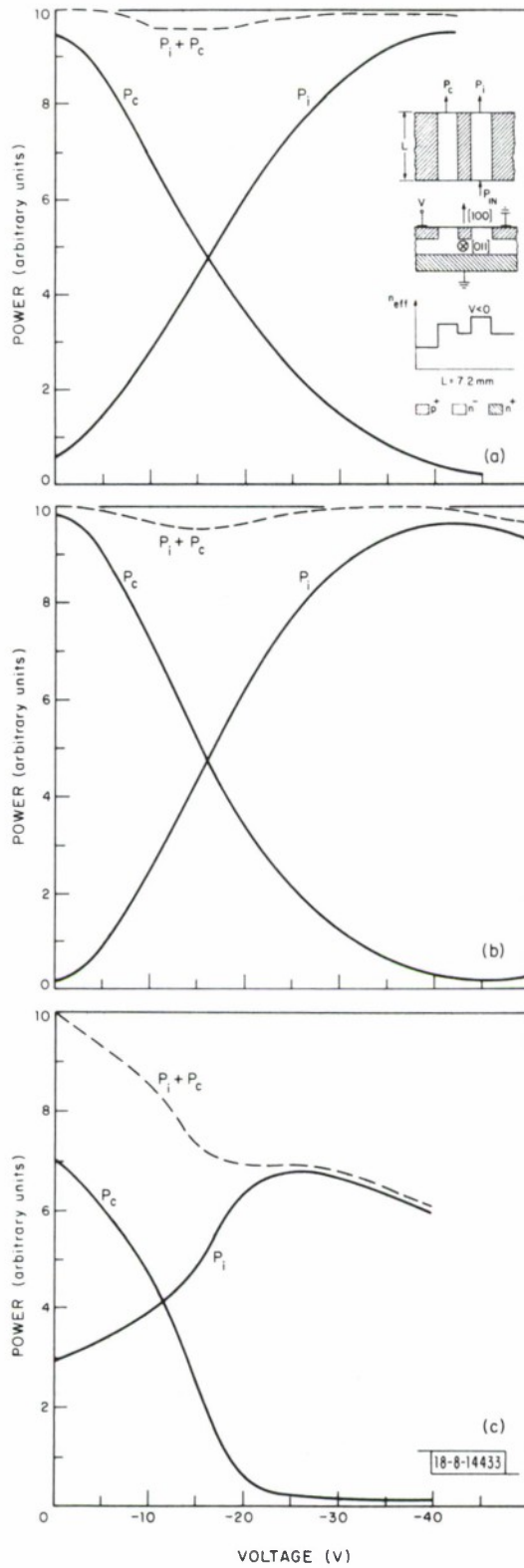
Fig. I-7. Power vs bias for each guide of a directional coupler switch for (a) 1.15 μm, (b) 1.06 μm, and (c) 0.92 μm. Diagrams to right in (a) illustrate, from top to bottom, the optical arrangement, biasing scheme, and a schematic effective index profile that apply to all three figures.

layers 5 to 6 μm thick. As can be seen, the coupling length increases with decreasing wave-length, with the largest change between 1.06 and 0.92 μm, where an ~50-percent increase in L_c is measured. The uncertainty in the measured values of L_c is ±5 percent. A simple theory based on the change of refractive index with wavelength in the different sections of the guides has been used to explain the observed variation of coupling length with wavelength and epitaxial thickness, and will be presented in a subsequent report.

Experimental switching results for λ = 1.15, 1.06, and 0.92 μm are shown in Fig. 1-7(a-c) for a device cleaved to its 1.06-μm coupling length of 7.2 mm. The device was fabricated on (100)-oriented material, and propagation was in the [011] direction to minimize power loss.[4,5] The guides were 8.5 μm wide with a 4-μm spacing, and the epitaxial layer was 4.8 μm thick. Figure 1-7 indicates the variation with bias of the output power P_i from the input guide, P_c from the coupled guide, as well as the total power $P_i + P_c$. The diagrams in the right portion of Fig. 1-7(a) show that light was incident in the guide furthest from the biased p^+ region. Also shown is a schematic effective index profile at an arbitrary reverse voltage that illustrates the reduction of guide index with bias. Figure 1-7(a) shows the results for λ = 1.15 μm. Here, 13-dB power isolation is obtained at zero bias, and 16-dB isolation is obtained at a switching voltage of −42 V. The total output power is constant to $\leqslant$0.2 dB. The relatively low zero-bias power isolation is due to a device length ~10 percent greater than the 1.15-μm coupling length. At 1.06 μm, the device exhibited 17-dB isolation at both zero bias and the switching voltage of −43 V (Ref. 5), as shown in Fig. 1-7(b). The total output power is constant to $\leqslant$0.2 dB. The small dip in total output power at biases around −15 V that occurs at both 1.06 and 1.15 μm is not fully understood. It could be a measurement effect resulting from movement of mode centers toward the middle of the coupler at these intermediate biases. In Fig. 1-7(c), the 0.92-μm results are presented. At zero bias, poor power isolation (~5 dB) was obtained because the device length was only ~65 percent of the coupling length. However, the data indicate that light in the coupled guide can be extinguished to yield 18-dB isolation at a switching voltage of −30 V. The total power decreased by 1.7 dB, which could be attributed to electroabsorption effects.[6] Electroabsorption effects were more pronounced if bias was applied adjacent to the input guide. In this case, the light output from both guides was extinguished for biases of approximately −30 V. If one assumes an extinction of 20 dB, an induced absorption of α ~ 6 cm^{-1} is implied which corresponds[6] to an electric field of ~3 × 10^4 V/cm. It is difficult to make an exact comparison with these calculated values since the electric fields in the guide region are fringing fields, but the order of magnitude appears to be correct. Nevertheless, acceptable switching behavior can be obtained if bias is applied near the coupled guide as shown in Fig. 1-7. This biasing method isolates the high-field regions from the optical power as much as possible.

The wavelength dependence of L_c in GaAs $p^+n^-n^+$ directional couplers has been described. We found that increases in L_c as the wavelength decreased can be attributed to changes in effective guide index. Switching results indicate that power isolation of 17 dB at zero bias can be obtained for devices equal to a coupling length, and that 16- to 18-dB power isolation in the input guide over the 0.92- to 1.15-μm wavelength range can be obtained with the appropriate bias. [It should be noted that improved switching behavior with >22-dB isolation at both 1.06 and 1.15 μm has been obtained using a GaAs switch with a $\Delta\beta$ reversal (see Sec. B above).] Finally, we found that electroabsorption effects influence switch power output at 0.92 μm and presumably at other wavelengths near the GaAs band edge.

<div align="right">

F. J. Leonberger
J. P. Donnelly
C. O. Bozler

</div>

D. n- AND p-TYPE LAYERS IN InP PRODUCED BY ION IMPLANTATION

Ion implantation in InP has the potential of being of significant practical importance in the fabrication of optoelectronic and microwave devices. Although implantation of Si^+ and Se^+ in $InAs_xP_{1-x}$ ($x \geqslant 0.2$) has been reported,[7] there has been little published work on ion implantation in InP. In our last report,[8] we gave a brief summary of our initial results in this area. In this section, we report in more detail our results on the use of ion implantation to create both n- and p-type layers in InP. Ions of Se^+ and Si^+ implanted at 400 keV were used to make n-type layers, while p-type layers were made with Be^+, Mg^+, and Cd^+ ions implanted at 50, 150, and 400 keV, respectively. Some implantations of Kr^+ were also made to investigate the nature of the residual implantation-induced damage. An encapsulation technique using pyrolytic phospho-silicate glass (PSG) was developed to reproducibly protect the samples at the required 700° to 750°C annealing temperatures.

The InP samples used in these experiments were cut from (111)-oriented crystals, polished and etched[9] in a 1:1:5:1 mixture of $HAc:HClO_4:HNO_3:HCl$. During implantation, they were held at either 77 K, room temperature, or 200°C, and were tilted with reference to the ion beam to minimize channeling. Prior to annealing, the samples were encapsulated with 2500 to 3000 Å of pyrolytic phosphosilicate glass (PSG) deposited at 250°C. Other coatings including pyrolytic SiO_2 and sputtered and pyrolytic Si_3N_4 were tried, but they generally cracked and/or peeled at temperatures above 700°C. The PSG was deposited in a "cold wall" reactor similar to that used to deposit pyrolytic silicon nitride.[10-12] Two inlet lines were used, one carrying 400 scc/min. of 0.2-percent PH_3 in N_2 and 125 scc/min. of 15-percent SiH_4 in N_2 further diluted in 4000 scc/min. of N_2, and the other carrying 140 scc/min. of O_2 diluted in 4000 scc/min. of N_2. After the flows reached a steady state, the InP was heated rapidly by means of a low mass graphite heater strip to 250°C to initiate deposition of the PSG. It took approximately 3.5 min. to deposit 2500 Å of PSG, after which the sample was rapidly cooled. The composition of the PSG was determined by wet chemical analysis to be nominally 7.84-wt% P (17.96-wt% P_2O_5), for which composition the thermal expansion coefficient has been reported[13] to be about 3.4×10^{-6}/°C, as compared with 4.5×10^{-6}/°C for InP.

Annealing was carried out in flowing nitrogen at temperatures of 700° to 750°C for 1 to 15 min. Anneal times of 5 to 15 min. gave the same results. Microalloyed-plated Au-Sn was used to contact n-type layers, while microalloyed-evaporated Au-Zn or Au-Mg was used to contact the p-type regions. Cloverleaf patterns were then etched in the implanted layers to facilitate Hall measurements of the van der Pauw type.[14]

To test the effectiveness of the PSG encapsulation on the InP, some annealing experiments were performed on unimplanted samples of high-resistivity ($\rho \geqslant 10^7$ Ω-cm) Fe-doped InP. As in high-resistivity Cr-doped GaAs (Ref. 15), variations in annealing results among samples from different ingots of the Fe-doped InP were observed. For crystal 25RH, unimplanted samples were either coated with PSG directly after etching or first heated to 200°C in the implantation system to duplicate the conditions of a hot implant. In either case, 15-min. anneals at temperatures up to 750°C produced no measurable conducting layers on the unimplanted samples. Following a 775°C anneal, however, n-type surface layers with sheet electron concentrations of 2×10^{11} cm^{-2} were observed. Samples from another crystal, HPOZ9, when heated to 200°C and then encapsulated and annealed at 750°C for 15 min., had n-type skins with $n \approx 4 \times 10^{11}$ cm^{-2}. As discussed below, this latter crystal also behaved somewhat differently for low-dose Se^+ implants.

To assess the possible effects of residual damage on the implantation, 400-keV Kr^+ ions were implanted into Fe-doped InP crystal 25RH. On samples implanted with 1×10^{12} cm^{-2} Kr^+ at either room temperature or 200°C and annealed at 750°C, there were no measurable conducting surface layers. For samples implanted with 1×10^{14} cm^{-2} Kr^+ and annealed at 750°C, however, n-type surface layers with concentrations of $(4 \text{ to } 6) \times 10^{12}$ cm^{-2} were observed when the implant was carried out at room temperature, while concentrations of only $(0.6 \text{ to } 3) \times 10^{11}$ cm^{-2} were observed when the implants were carried out at 200°C. The sheet concentrations measured on the samples annealed at 750°C were much lower than those observed on unannealed samples, and were also generally lower than those on samples annealed at 700° and 725°C. From these results, it appears that residual damage in InP is n-type and, at least for heavy ions, this n-type damage can be reduced substantially by implanting at 200°C. In recent experiments, however, there is some indication that some damage-enhanced diffusion or decomposition may take place during a 200°C implant. There may therefore be an optimum implant temperature between room temperature and 200°C which minimizes the formation of n-type skins with heavy ion bombardment.

Implantations of the donor ions Si^+ and Se^+ were performed with substrates at room temperature and 200°C. For a dose of 1×10^{14} cm^{-2} of either ion, higher sheet carrier concentrations N_s and mobilities μ_s were obtained for the higher temperature implants. With Se (the experiments were not performed for Si^+), both parameters also increased with increasing anneal temperature between 700° and 750°C. For samples implanted with 1×10^{14} cm^{-2} Se at room temperature, N_s and μ_s were 4.8×10^{13} cm^{-2} and 1170 cm^2/V-sec, respectively, following a 700°C anneal, and 6.0×10^{13} cm^{-2} and 1470 cm^2/V-sec, respectively, following a 750°C anneal. For similar samples implanted at 200°C, N_s and μ_s were 6.9×10^{13} cm^{-2} and 1710 cm^2/V-sec, respectively, following a 700°C anneal, and 7.9×10^{13} cm^{-2} and 1810 $cm^2/$V-sec, respectively, following a 750°C anneal.

Figure I-8 shows the measured sheet carrier concentration and mobility vs Si^+-ion dose for Fe-doped InP samples (25RH) implanted at 200°C and annealed at 750°C for 15 min. For comparison, the results of a room-temperature 1×10^{14} cm^{-2} Si implant are also shown. The dashed line represents 100-percent electrical activation of the implanted silicon. The highest measured activation of 80 percent was obtained for a dose of 3×10^{13} cm^{-2}, while the lowest sheet resistivity, 15 $\Omega/\square$, was the result of a dose of 1×10^{15} cm^{-2}. For doses $\leqslant 1 \times 10^{13}$ cm^{-2}, the percentage activation and the mobility no longer increased with decreasing dose. This is believed to be due to an excess of compensation in the Fe-doped InP ingot 25RH.

The results for Se^+ are shown in Fig. I-9 for two different Fe-doped InP samples implanted at 200°C and annealed at 750°C. The results on samples of ingot 25RH are very similar to those obtained on the same material with Si^+ (Fig. I-8). At a dose of 1×10^{14} cm^{-2}, 79 percent of the implanted Se is electrically active; at a dose of 1×10^{15} cm^{-2}, the sheet resistivity is 16 $\Omega/\square$; and for doses $\leqslant 1 \times 10^{13}$ cm^{-2}, the percentage activation and mobility decrease with decreasing dose. On samples from crystal HPOZ9, the results are identical to those obtained on 25RH for doses $\geqslant 1 \times 10^{14}$ cm^{-2}. For low doses, however, the percentage activation increases with decreasing dose, apparently becoming greater than 100 percent for a dose of 1×10^{12} cm^{-2}. This is consistent with the above-mentioned observation that heated and annealed samples of this crystal showed n-type surface layers even when unimplanted. The variations for low doses between different Fe-doped InP ingots are similar to those observed between Cr-doped GaAs ingots[15-17] and are currently under further investigation.
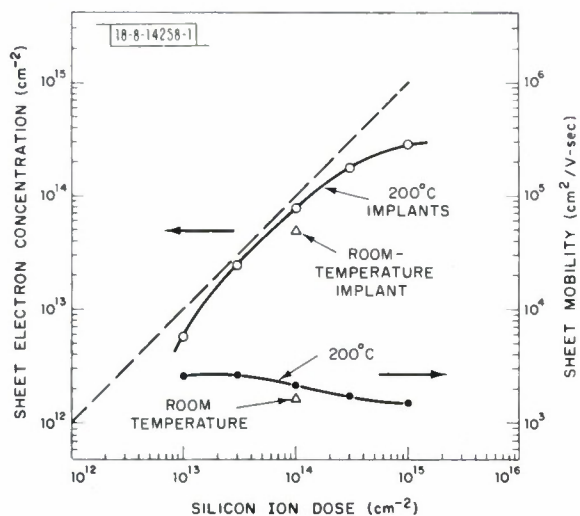
Fig. I-8. Sheet electron concentration and mobility vs dose for 400-keV Si^+-implanted Fe-doped InP crystal 25RH. Samples were implanted bare, encapsulated with PSG, and annealed at 750°C for 15 min.

Fig. I-9. Sheet electron concentration and mobility vs dose for two different Fe-doped InP ingots implanted with 400-keV Se^+ ions. Samples were implanted bare, encapsulated with PSG, and annealed at 750°C for 15 min.
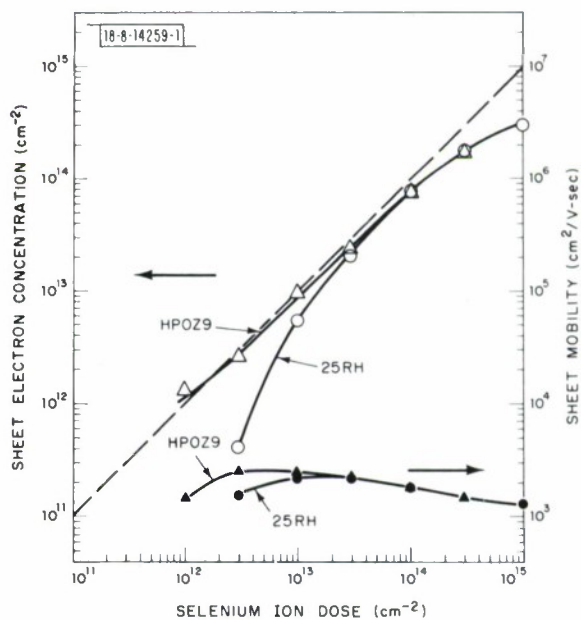
Ions of Cd^+, Mg^+, and Be^+ were employed to create p-type layers. Fe-doped (25RH) substrates were used exclusively, except for a few Mg implants into n-type material. Table I-1 lists the pertinent results. For samples implanted with 1×10^{14} cm^{-2} Cd^+, higher sheet hole concentrations were observed when the implants were carried out at 200°C. This is probably due to the lower residual n-type damage obtained when using heated substrates, in agreement with the Kr^+ results. Note that the concentration also increased with anneal temperature, reaching 3.7×10^{13} cm^{-2} with a mobility of 91 cm^2/V-sec for a 200°C implant annealed at 750°C for 15 min.

For Mg^+ ions the results are the reverse of those for Cd^+, with the sheet hole concentration for a 1×10^{14} cm^{-2} implant being higher on samples implanted at room temperature than at 200°C. Furthermore, there was not as significant an increase in N_s with anneal temperature as observed for Cd^+. The highest sheet concentration, 5.2×10^{13} cm^{-2}, was observed on a sample implanted with 1×10^{14} cm^{-2} Mg^+ and annealed at 750°C. For still higher Mg^+ doses ($\geqslant 3 \times 10^{14}$ cm^{-2}), the measured sheet concentrations were approximately the same for room-temperature and 200°C implants and were smaller than that obtained for 1×10^{14} cm^{-2} room-temperature implants. These results and the reasons for their difference from those for Cd^+ are not presently understood. Samples implanted at 77 K gave results identical to those obtained at room temperature, and similar results were also obtained for implants made into n-type substrates ($n \approx 4 \times 10^{16}$ cm^{-3}).

A limited number of Be^+ implants were made and only into room-temperature substrates. The sheet hole concentrations of samples implanted with 1×10^{14} cm^{-2} Be^+ at 50 keV did not vary much for anneal temperatures between 700° and 750°C and were about 3×10^{13} cm^{-2}.

<div style="text-align: right">

J. P. Donnelly
C. E. Hurwitz

</div>

TABLE 1-1

SHEET HOLE CONCENTRATION (N_s) AND MOBILITY (μ_s) FOR BERYLLIUM, MAGNESIUM, AND CADMIUM IMPLANTS IN InP†

Ion	Energy (keV)	Dose (cm^{-2})	Anneal Temperature (°C)	25°C Implants		200°C Implants	
				N_s (cm^{-2})	μ_s ($cm^2/V\text{-}sec$)	N_s (cm^{-2})	μ_s ($cm^2/V\text{-}sec$)
Be$^+$	50	1×10^{14}	700	3.5×10^{13}	83	—	—
			725	2.9×10^{13}	100	—	—
			750	3.3×10^{13}	81	—	—
Mg$^+$	150	1×10^{14}	700	4.5×10^{13}	68	—	—
			725	4.4×10^{13}	92	1.5×10^{13}	95
			750	5.2×10^{13}	83	—	—
Cd$^+$	400	1×10^{14}	700	4.3×10^{12}	47	2.3×10^{13}	69
			725	—	83	—	—
			750	1.6×10^{13}	90	3.7×10^{13}	91

† All samples were implanted bare, encapsulated with PSG, and annealed for 15 min. at the specified temperature.

REFERENCES

1. Solid State Research Report, Lincoln Laboratory, M.l.T. (1977:2), p. 1.

2. F. J. Leonberger and C. O. Bozler, Appl. Phys. Lett. 31, 223 (1977).

3. Solid State Research Report, Lincoln Laboratory, M.l.T. (1976:2), p. 4, DDC AD-A030861/9.

4. Ibid. (1976:3), p. 1, DDC AD-A034647/8.

5. F. J. Leonberger, J. P. Donnelly, and C. O. Bozler, Appl. Phys. Lett. 29, 652 (1976), DDC AD-A037627/7.

6. G. E. Stillman, C. M. Wolfe, C. O. Bozler, and J. A. Rossi, Appl. Phys. Lett. 28, 544 (1976), DDC AD-A029284/7.

7. D. E. Davies, T. K. Kennedy, and L. F. Lowe, Electron. Lett. 11, 462 (1975).

8. Solid State Research Report, Lincoln Laboratory, M.l.T. (1977:2), p. 12.

9. R. Becker, Solid-State Electron. 16, 124 (1973).

10. J. P. Donnelly, W. T. Lindley, and C. E. Hurwitz, Appl. Phys. Lett. 27, 41 (1975), DDC AD-A016690/0.

11. C. O. Bozler, J. P. Donnelly, R. A. Murphy, R. W. Laton, R. W. Sudbury, and W. T. Lindley, Appl. Phys. Lett. 29, 123 (1976), DDC AD-A030622.

12. J. P. Donnelly, Chapter 4 in Gallium Arsenide and Related Compounds (St. Louis) 1976, edited by L. F. Eastman (Institute of Physics, London, 1977), p. 166.

13. B. J. Baliga and S. K. Ghandhi, in Technical Digest of International Electron Device Meeting, Washington, D. C., 1973 (IEEE, New York, 1973), p. 256.

14. L. J. van der Pauw, Philips Res. Rep. 13, 1 (1958).

15. J. P. Donnelly, C. O. Bozler, and W. T. Lindley, Solid-State Electron. 20, 273 (1977).

16. W. Kellner, H. Kniepkamp, D. Ristow, M. Heinzle, and H. Boroffka, Solid-State Electron. 20, 459 (1977).

17. C. A. Stolte, in Technical Digest of International Electron Device Meeting, Washington, D. C., 1975 (IEEE, New York, 1975), p. 585.

II. QUANTUM ELECTRONICS

A. NdP$_5$O$_{14}$ Q-SWITCHED LASER OPERATION

We have continued the development of the previously reported flash-lamp-excited NdP$_5$O$_{14}$ laser[1] with the addition of an intra-cavity passive Q-switch. The Q-switch cell had 12.5-mm-diameter windows separated by a spacer ring 0.7 mm thick. The outer surfaces of the windows were antireflection-coated at 1.05 μm, and the Q-switch dye solution was bis (4-diethylaminodithiobenzil) nickel[2-4] (Kodak 14617) dissolved in toluene. Two tubes for filling and emptying the dye cell allowed interchange of different dye concentrations without affecting the alignment of the laser cavity. The cell was attached to the output mirror mount, so its alignment was done simultaneously with that of the output mirror.

The procedure that was used in the Q-switch measurements was to first fill the cell with pure toluene, and maximize the laser output energy under long-pulse operation. Then the output-pulse behavior was measured with different concentrations of the Q-switch dye, ranging from 0.5×10^{-5} to 3.0×10^{-5}M solutions. This procedure was repeated for several output mirror transmissions.

For the various combinations of output mirror transmission and dye concentration, there was generally a range of input energies for which single Q-switched pulse output was obtained. Within this range, the output energy was constant. For input energies below this range, the laser was below threshold; for higher energies, multiple pulses occurred, corresponding to repetitive bleaching and recovery of the dye. The tendency for multiple pulsing was larger with dilute dye solutions and low mirror transmissions.

Maximum single pulse output was obtained with 20-percent output transmission and the 3.0×10^{-5}M dye solution. Round-trip loss caused by the unbleached dye solution was estimated to be 30 percent. Laser threshold was at 880 mJ, and with 1-J lamp input energy, Q-switched pulses from 1.5 to 2.0 mJ were obtained, with a duration (FWHM) of ~6 nsec. The fluctuation in output energy is attributed partially to operation close to threshold, but primarily to the fluctuation of the multimode transverse intensity distribution, which causes different degrees of dye saturation, even though the corresponding long-pulse energy is constant. This short-pulse output was about 30 percent of the long-pulse energy, 6.4 mJ, obtained with the same output mirror. (This output mirror had greater transmission than optimum for long-pulse operation, since higher energies were obtainable at 1-J input with a 10-percent transmission output mirror.) Efforts are now under way to improve the transverse-mode quality of the laser in order to obtain more reproducible performance.

<div style="text-align:right">

S. R. Chinn
W. K. Zwicker[†]

</div>

B. TRANSITION-METAL ION SOLID STATE LASERS

We are currently investigating lasers using transition-metal-doped crystals as the active media. Such lasers are potentially interesting tunable sources at a variety of wavelengths in the near-infrared; the tunability results from strong phonon coupling to the electronic states of the ions, which leads to typically large (>500 cm^{-1}) gain linewidths. For example, previous

---

[†] Philips Laboratories, Briarcliff Manor, NY.

work using MgF_2:Ni crystals showed that the laser oscillation could be achieved in a number of wavelength segments between 1.62 and 1.84 μm (Ref. 5).

We have concentrated our efforts initially on MgF_2:Ni because that crystal exhibited the lowest threshold in CW, lamp-pumped operation for a variety of systems studied earlier.[5] Also, there is a fortunate coincidence between the peak of the lowest-energy absorption band of MgF_2:Ni and the 1.318-μm line of the Nd:YAG laser, which permits use of this line for longitudinal pumping of reasonably short crystals. High-optical-quality crystals have been grown[6] which appear to have very low intrinsic losses. We have observed laser operation in a system employing a 2-cm-long crystal doped with about 1-wt% Ni. The 12.5-cm-long laser cavity consisted of one end of the crystal polished flat and coated for high reflectivity around 1.65 μm, and a 25-cm-radius concave mirror coated for 0.2-percent transmission around 1.65 μm. The uncoated end of the crystal was polished flat and parallel to the coated end. The crystal was conduction-cooled in an LN_2 Dewar, and the Dewar window in the cavity was AR-coated. Figure II-1 shows the output of this laser when pumped by the chopped focused output of a 1.318-μm Nd:YAG laser. The latter output appears as rectangular pulses in the lower portion of the photograph. The spiking nature of the output is characteristic of lasers with long upper-state lifetimes; the long time delay between the onset of pumping and laser action is almost entirely the time required for the upper-state population (lifetime 12 msec) to reach the threshold condition. Oscillation occurred around 1.63 μm; the lowest threshold pump power observed, 3.5 W, was higher than optimum because of the large number of transverse modes present in the pump laser output, which limited focused intensity. We are currently working to reduce the number by modifying the resonator geometry of the pump laser.

-8-14400-1

Fig. II-1. Output of MgF_2:Ni laser just above threshold, with chopped pump laser signal visible. Spiked output pulses are off-scale and not time-resolved.

There are a number of other combinations of dopant and host crystal which warrant further investigation. We have grown a crystal of MgF_2:Co and measured the near-infrared absorption spectrum. As in MgF_2:Ni, the lowest energy absorption band peaks around the 1.318-μm Nd:YAG line. The expected range of oscillation frequencies is at longer wavelengths than MgF_2:Ni, however.[5] MgO:Ni or MgO:Co can be pumped by the strong 1.06-μm Nd:YAG line[7] and would oscillate around 1.3 μm, but it is unclear if large optical-quality crystals of these materials can be obtained.

P. F. Moulton   T. B. Reed
A. Mooradian   R. E. Fahey

16

C. MINI-TEA CO$_2$ LASER

The desirability of obtaining compact sources of pulsed CO$_2$ laser radiation which can be used in conjunction with nonlinear crystals, such as CdGeAs$_2$, to generate additional frequencies was discussed in the previous Solid State Research report.[8] For effective monitoring of molecular effluents at long distances, it is desirable for this source to have a repetition rate above 100 Hz with tens of millijoules pulse energy.

To obtain such a source we have designed and constructed a mini-TEA laser conceptually similar to the one recently reported by Bua and Rudko,[9] but differing considerably in detail. Our initial unit contains Rogowski profile aluminum electrodes with a planar region 4 × 115 mm and a 4-mm spacing between electrodes. The laser body is constructed of aluminum top and bottom plates, lucite sides, and vespel spacers. Its overall length, including Brewster windows but exclusive of mirrors, is less than 30 cm. A printed-circuit sparkboard is used for UV preionization, and with it we have obtained essentially arc-free laser action at atmospheric pressure with a flowing gas system and no external cooling.
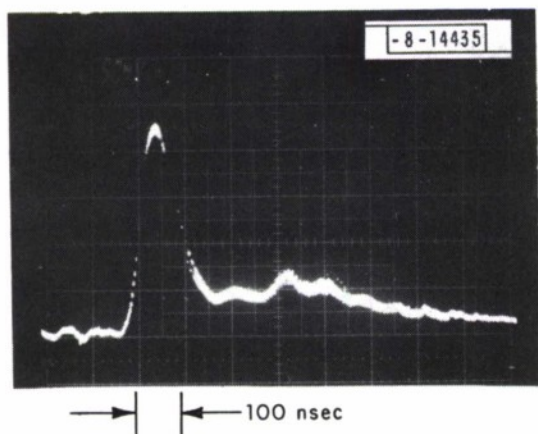
Fig. II-2. Mini-TEA CO$_2$ laser output pulse.

Pulse energies of 38 mJ and repetition rates over 10 Hz have been obtained. This output corresponds to an energy extraction of 20 J/liter. Since the pulse rate limitations are due to peripheral components, significant improvement in these results is anticipated. The pulse output obtained with this unit for a CO$_2$:N$_2$:He gas flow ratio of 1:1.2:8 is shown in Fig. II-2, which indicates that a major fraction of the energy is contained in the initial 100-nsec-wide spike.

N. Menyuk
P. F. Moulton

D. EFFICIENT INFRARED THIRD-HARMONIC GENERATION IN CRYOGENIC LIQUID CO MIXTURES

We recently reported third-harmonic (TH) generation of CO$_2$ laser radiation in cryogenic liquid CO mixtures.[10] Presently, we are using the TH process as a means for studying these mixtures and are evaluating possible limiting effects in TH generation. The CO was diluted in solvents such as O$_2$, Ar, and N$_2$ which have negligible dispersion between the pump and the TH frequency. The purpose was to increase the TH coherence length. Maximum TH conversion occurs when the coherence length is approximately equal to the confocal parameter of the focused CO$_2$ laser beam. Besides reducing the dispersion, the solvents also affect significantly the two-photon resonance enhancement of the third-order susceptibility, $\chi^{(3)}$, for CO. This has been

17

investigated by measuring both the position and the linewidth of the vibrational two-photon resonance in CO using spontaneous polarized Raman scattering (see Sec. E below where these results are discussed in more detail).

Most of our TH experiments have been performed using CO-O_2 mixtures. N_2 was not used as a diluent because of the reduced resonance enhancement, and CO-Ar mixtures were not used extensively because of experimental problems arising from the small temperature difference between the liquid Ar freezing and boiling points at 84.0 and 87.5 K, respectively.

For CO-O_2 solutions, $\chi^{(3)}$ is approximately constant at relative CO concentrations higher than 0.1, because at higher concentrations the effect of increasing the CO density is offset by an increasing resonance denominator. This was verified for a CO-O_2 solution in an experiment using the 25-cm-long Dewar and with the pump beam focused to a confocal parameter of 4.8 cm. The TH conversion efficiency was optimized at different CO concentrations by dissolving SF_6 in the solution. Since SF_6 has a positive dispersion between the TH and the pump frequency, adding SF_6 increases the relative CO concentration at which the optimum coherence length for TH generation is obtained. At relative CO concentrations between 0.1 and 0.4, the maximum TH conversion efficiency was found to be approximately independent of CO concentration.

The TH output power is proportional to the input power cubed up to the laser-induced-breakdown threshold. We have observed no limiting effects other than the laser-induced breakdown. In the tight focusing limit, i.e., for a confocal parameter much shorter than the cell length, maximum TH conversion efficiency is expected to increase with the confocal parameter squared when the laser-induced-breakdown threshold limits the conversion efficiency. Experimentally, we observed an increase in the TH conversion efficiency from 0.3 to 2 percent when the confocal parameter was increased from 0.8 to 4.8 cm. This increase is somewhat smaller than expected from simple theory. This occurs because the laser-induced energy density breakdown threshold for the R(6) pump line decreases with increasing confocal parameter. The breakdown threshold also shows a frequency dependence. It is lowest for the R(6) pump line and increases with increasing two-photon resonance frequency mismatch. The resonance does not appear to be as sharp, however, as that of the polarized part of the two-photon absorption resonance.

In addition to the above experiments, we have examined theoretically several effects that might potentially limit the TH conversion efficiency.

1. <u>Power Broadening of the Resonant Transition:</u>— The calculated maximum power broadening of the vibrational two-photon resonance is less than 0.05 cm^{-1}, and is therefore negligible compared with the 0.6-cm^{-1} linewidth.

2. <u>Two-Photon Resonant Stark Effect:</u>— This frequency shift is of the same order of magnitude or smaller than the power-broadened linewidth, and is therefore negligible.

3. <u>One-Photon Nonresonant Stark Effect:</u>— The nonresonant Stark effect should frequency-shift both the lower and upper levels of the vibrational two-photon transition in the same direction and by the same magnitude. The estimated maximum frequency shift of the lower level is less than 0.1 cm^{-1}, and is therefore negligible.

4. <u>Two-Photon Absorption:</u>— At high TH power-conversion efficiencies there is some two-photon absorption. In the tight focusing limit assuming exact two-photon resonance, the TH power-conversion efficiency can be written, neglecting pump depletion effects, as

18

$$P_3/P_1 = 1.6\left(\frac{\Delta P_1}{P_1}\right)^2$$

where $\Delta P_1/P_1$ is the relative two-photon absorption in the cell. For 10-percent TH power-conversion efficiency, the two-photon absorption is therefore 25 percent. By tuning slightly off the two-photon absorption resonance, it is possible to obtain a higher TH conversion efficiency for the same relative two-photon absorption, since the resonance lineshapes differ for the two processes. The two-photon absorption in liquid CO does not break the phasematching condition, since the dispersion per molecule is identical for excited and ground state molecules within the harmonic oscillator approximation.

5. Two-Photon Resonant Kerr Effect:— At exact two-photon resonance, the resonant Kerr effect vanishes. When the second harmonic of the pump frequency is either below or above the CO transition frequency, the resonant Kerr effect changes the index of refraction at the pump frequency causing the pump beam to respectively focus or defocus. When the pump frequency is tuned off-resonance in order to maximize the Kerr effect, the TH power-conversion efficiency in the tight focusing limit can be expressed as

$$P_3/P_1 = 3.2\varphi^2$$

where φ is total phase change due to the Kerr effect measured along the beam axis when the pump beam traverses the TH cell. A TH conversion efficiency of 10 percent corresponds to a phase change of only 0.18 rad, which means that the resonant Kerr effect is negligible.

6. Stimulated Brillouin Scattering:— For 100-nsec pump pulses, the stimulated Brillouin scattering does not reach steady state, and our preliminary calculations of the transient Brillouin gain indicate that this process is negligible. Experimentally, we have looked for backward Brillouin scattering, and the results have been negative.

Finally, it should be emphasized that two-photon resonant TH generation is not limited to a single CO_2 input frequency. With two incident CO_2 frequencies at ω_1 and ω_2, output is generated efficiently at $2\omega_1 + \omega_2$ when either $2\omega_1$ or $\omega_1 + \omega_2$ satisfies the two-photon resonance condition.

<div align="right">

H. Kildal
S. R. J. Brueck

</div>

E. POLARIZED VIBRATIONAL RAMAN-SCATTERING LINESHAPE PARAMETERS IN LIQUID CO AND LIQUID CO MIXTURES

The efficient nonlinear frequency conversion of CO_2 laser light in liquid $CO-O_2$ mixtures, which was discussed in Sec. D above and in Ref. 10, arises because of a two-photon (Raman) resonance between the CO vibrational mode and the second harmonic of the CO_2 laser line at 1069 cm^{-1}. For a complete understanding and optimization of this nonlinear process, an independent measurement of the parameters (linewidth and frequency) of this two-photon resonance is required. We have therefore carried out a Raman-scattering measurement of these parameters for $CO-O_2$, $CO-N_2$, and CO-Ar mixtures.

The experiment was carried out with a conventional Raman-scattering arrangement. An Ar laser operating at 514.5 nm (~300 mW power level) with an internal etalon to ensure single longitudinal mode operation was focused into a cryogenic liquid cell containing the liquid CO-diluent mixture. A separate liquid bath fixed the sample temperature at 77 K (87 K for the

CO-Ar measurements). Backscattered Raman light was collected at a small angle from the incident light and passed through a pressure-scanned Fabry-Perot interferometer (2.587 cm^{-1} free spectral range), and detected with a small area (1×10^{-3} cm^2) photomultiplier operated with photon counting electronics. The interferometer free spectral range was calibrated in the spectral region of the Raman signal using the 577- and 579-nm lines of an Hg discharge lamp. For measurements of the absolute Stokes shift, the Ar laser was tuned to excite the intense fluorescence from an I_2 cell which occurs for a pump frequency shifted approximately 1 GHz toward the blue from the Ar laser line center[11] at 514.533 nm. Polarization measurements indicated that the depolarized scattering component contributed only a uniform background to the narrow polarized spectral feature.

Figure II-3 shows the measured linewidth (bottom) and Stokes shift (top) measurements for $CO-N_2$ and $CO-O_2$ solutions as a function of the relative (to neat CO liquid) CO peak absorbance at the second vibrational overtone absorption band at 1.575 μm. The absolute Stokes shift for a pure CO liquid was measured several times as described above, and the resultant value for the CO two-photon resonance frequency was 2138.54 ± 0.05 cm^{-1}. (The correct order of the Fabry-Perot was chosen by requiring a close two-photon resonance with the CO R(6) line as was determined in the nonlinear optics experiments.[10]) This result is 0.52 ± 0.05 cm^{-1} higher in frequency than the second harmonic of the CO_2 laser R(6) line at 1069.01 cm^{-1}. It is clear
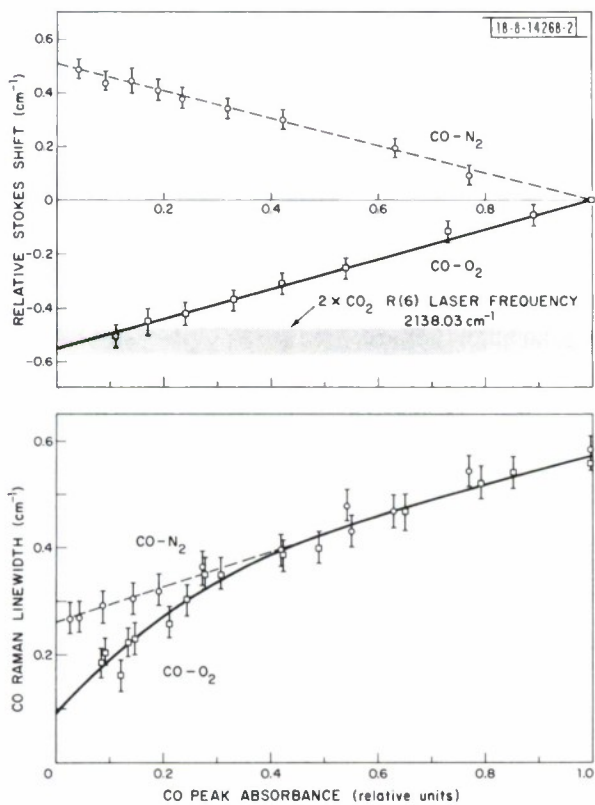
Fig. II-3. Relative Stokes frequency shift (top) and linewidth (bottom) of CO polarized vibrational two-photon linewidth for liquid $CO-O_2$ and $CO-N_2$ solutions at 77 K. Absolute Stokes frequency measurement is indicated by shaded region at 2138.03 cm^{-1} [2 × R(6) of CO_2 laser 9.6-μm branch].
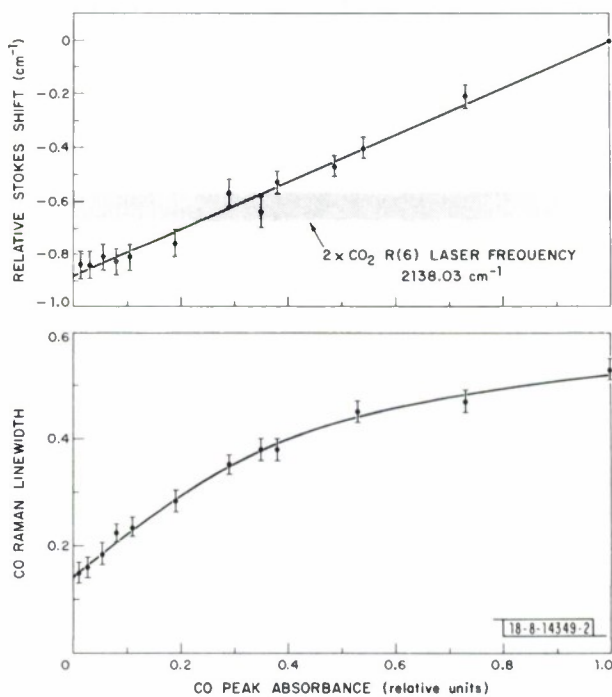
Fig. II-4. Relative Stokes frequency shift (top) and linewidth (bottom) of CO polarized vibrational two-photon linewidth for liquid CO-Ar solutions at 87 K. Absolute Stokes frequency measurement is indicated by shaded region at 2138.03 cm^{-1} [2 × R(6) of CO_2 laser 9.6-μm branch].

that the $CO-O_2$ solution is in two-photon resonance with the CO_2 laser R(6) line at a CO mole fraction of approximately 0.05. This resonance coupled with the narrow CO linewidth results in the large nonlinear susceptibility of $CO-O_2$ solutions as compared with $CO-N_2$ solutions.

Figure II-4 shows similar results for liquid CO-Ar solutions at 87 K. At this temperature the pure CO resonance is shifted to 2138.64 ± 0.05 cm^{-1}, and the linewidth has decreased somewhat. The temperature dependence of the saturated liquid CO two-photon resonance was measured over the limited range from approximately 72 K to the 87-K liquid argon boiling point; Dewar pressure constraints precluded higher temperature measurements. Over the narrow temperature range, the Stokes shift varied linearly with temperature with a slope of $+0.013$ cm^{-1}/K. The linewidth decreased with increasing temperature from 0.65 ± 0.05 cm^{-1} at 72 K to 0.53 ± 0.05 cm^{-1} at 87 K.

For very dilute solutions of CO in various nonpolar solvents, the measured linewidths are comparable to, but somewhat larger than, the previously reported linewidths of the N_2 and O_2 resonances.[12] This is expected, since the mechanisms which have previously been identified in these latter cases depend only upon spectroscopic constants or Lennard-Jones interaction parameters which are similar for all three molecules, and on a correlation time which is a measure of the speed of fluctuation of the local molecular environment. It is evident from the increase in the linewidth as the CO concentration is increased that an additional broadening mechanism must become important at high CO densities. This is an inhomogeneous broadening that results from the effects on one CO molecule of the random dipolar electric fields of the other CO molecules in the liquid. A simple calculation of this broadening, which is reduced because of the rapid orientational fluctuations in the liquid, indicates that it is of the correct order of magnitude to explain the measured results.

S. R. J. Brueck

F. IR DOUBLE-RESONANCE STUDIES OF HIGHLY VIBRATIONALLY EXCITED SF_6

The demonstration of laser isotope separation in SF_6 by multiphoton processes[13,14] produced by high-intensity CO_2 TEA laser irradiation has generated considerable interest in the excitation processes involved. Subsequent experiments[15] in which two lasers, one operating well to the high-frequency side of the ν_3 mode absorption band, were used for dissociation have raised the question of the spectral dependence of the induced absorption in CO_2-laser-excited SF_6. We have used an infrared double-resonance technique to probe the ν_3 mode kinetics of SF_6 under intense CO_2 TEA laser excitation. The current measurements differ from most earlier double-resonance measurements in that the excitation intensities are substantially higher;[16,17] one recent study had roughly similar conditions.[18]

The double-resonance experiments employed a collinear geometry in which the pump beam from a grating-tuned CO_2 TEA laser and the probe beam from a line-tunable CW CO_2 laser were propagated through a 26-cm-long cell. Pump intensities ranged from 0.02 to 4 MW/cm^2; a 100-nsec pulse (FWHA) with no N_2 afterpulse provided a well-defined excitation function. The maximum pump intensity was well below the 20-MW/cm^2 level needed to cause dissociation. The probe and pump laser polarizations were orthogonal, allowing the use of polarizers to reduce the pump intensity on the exit side of the cell. The probe beam was passed through a 3/4-m double monochromator, and induced changes in cell transmission were observed using a Cu:Ge detector-signal averaging system having a risetime faster than 50 nsec. SF_6 gas pressures ranged from 0.010 to 0.25 Torr.
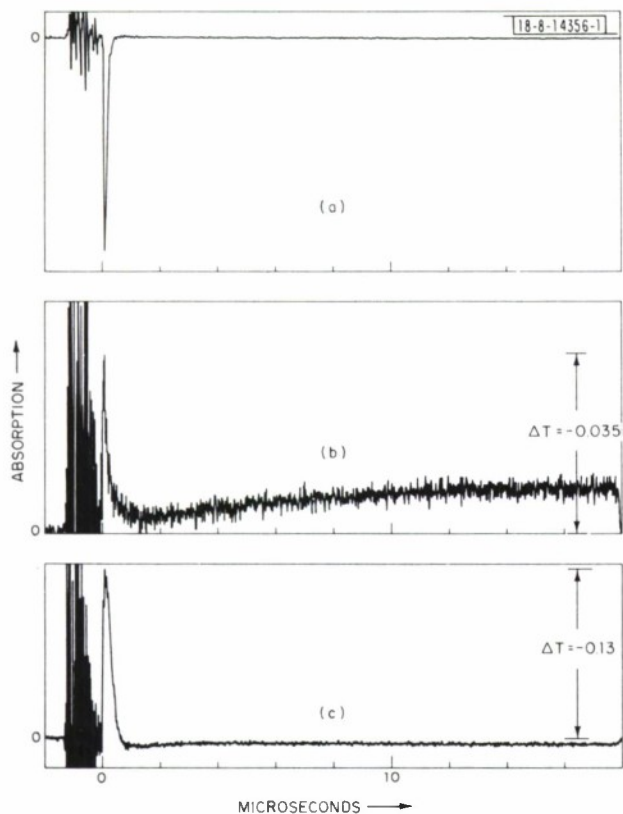
Fig. II-5. (a) Response of detector-signal averaging system to P(20) pump pulse at 944.2 cm^{-1}; (b) induced signal at 940.5 cm^{-1}, P(24). Pump intensity ~ 3 MW/cm^2, SF$_6$ pressure 0.010 Torr, cell length 26 cm. Average of 400 shots. (c) Induced signal at 947.7 cm^{-1}, P(16). Average of 200 shots. Other conditions as above.

Fig. II-6. (a) Linear absorption spectrum of SF$_6$ at 208 K. (b) Induced signal from 0.050 Torr SF$_6$ in a 26-cm cell at peak of P(20) pump pulse. Pump intensity ~ 3 MW/cm^2. (c) Induced spectrum 1 μsec after start of pump pulse. (d) Induced spectrum 10 μsec after start of pump pulse.

22
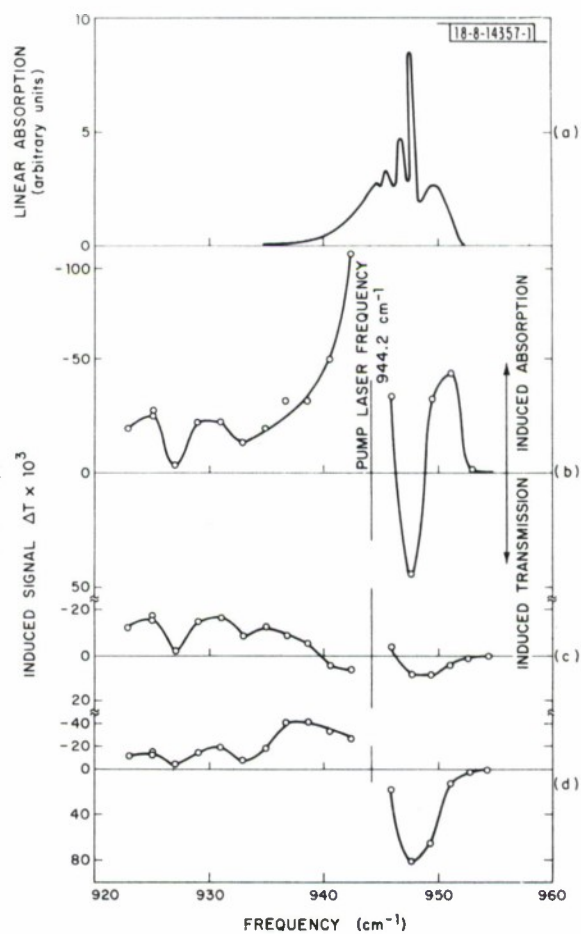
Figure II-5(a-c) shows the response of the detector-signal averaging system to the P(20) pump laser pulse, as well as the induced signals at the P(24) and P(16) CO_2 laser frequencies for an SF_6 pressure of 0.01 Torr. The induced absorption at P(24), on the low-frequency side of the ν_3 mode, has an initial spike with a pressure-independent shape that follows the pump pulse. The signal at P(16) also has a pressure-independent component, but it is slightly wider than the pump pulse; the initial induced absorption becomes induced transmission at longer times. Figure II-6(a-d) shows the linear absorption spectrum of SF_6, together with the spectrum of the induced absorption at three different times following the pump laser excitation. The induced absorption on the low-frequency side of the pump is initially strongest at the pump frequency, but after 1 μsec it is distributed more evenly to the red of the pump and finally, 10 μsec after the pump, it begins to show a peak near the pump line. At the pressure of this experiment, 0.050 Torr, rotational cross-relaxation occurs in 0.7 μsec (Ref. 17) and vibrational-vibrational relaxation in 30 μsec (Ref. 19), suggesting that changes in the induced spectrum in the first few microseconds after excitation may be due to rotational cross-relaxation.
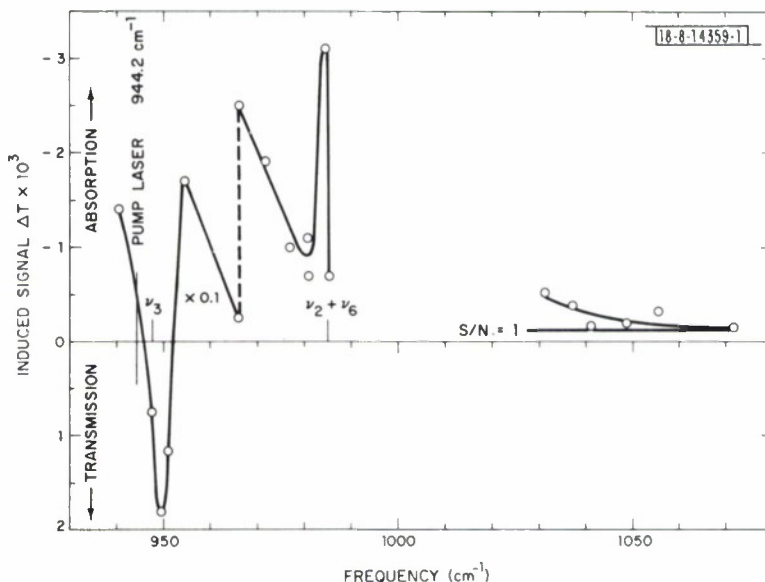
Fig. II-7. Spectrum of induced signal from 0.25 Torr SF_6 in 26-cm cell; P(20) pump ~3 MW/cm^2. Each point represents average of 1000 measurements.

Observation of induced absorption in the region 100 cm^{-1} to the blue of the ν_3 mode required the use of higher pressures, 0.25 Torr, and a slower, higher gain detector-preamplifier, which reduced the detector response time to 0.5 μsec. Figure II-7 shows the spectral dependence of the induced signal observed 1 μsec after the exciting pulse. Note that at a signal-to-noise ratio of unity a change in transmission of 10^{-4} can be detected, corresponding to a minimum detectable absorption of ~5×10^{-6} cm^{-1}. The sharp peak near 985 cm^{-1} is at the $\nu_2 + \nu_6$ combination band and is probably due to laser-induced hot bands of the type $\nu_3 \to \nu_2 + \nu_6 + \nu_3$.

The presence of a pressure-independent induced absorption that follows the pump pulse suggests a coherent excitation process (for example, "adiabatic following") in which molecules are excited to a number of levels of the ν_3 manifold from which transitions to other vibrational modes are possible.

T. F. Deutsch
S. R. J. Brueck

REFERENCES

1. Solid State Research Report, Lincoln Laboratory, M.I.T. (1977:2), p. 17; S. R. Chinn and W. K. Zwicker, Appl. Phys. Lett. $\underline{31}$, 178 (1977).

2. G. A. Reynolds and K. H. Drexhage, J. Appl. Phys. $\underline{46}$, 4852 (1975).

3. H. Lo, "Saturable Absorbing Materials for Q-Switching Neodymium Lasers," Final Report TR ECOM-0122-F, USAECOM, Fort Monmouth, N. J. (1972).

4. F. Kobylarz et al., Proceedings of 6th DoD Conference on Laser Technology, U. S. Air Force Academy, Colorado Springs, Colorado, 1976.

5. L. F. Johnson, H. J. Guggenheim, and R. A. Thomas, Phys. Rev. $\underline{149}$, 179 (1966).

6. Solid State Research Report, Lincoln Laboratory, M.I.T. (1977:2), p. 37.

7. J. E. Ralph and M. G. Townsend, J. Chem. Phys. $\underline{48}$, 149 (1968).

8. Solid State Research Report, Lincoln Laboratory, M.I.T. (1977:2), p. 21.

9. D. P. Bua and R. I. Rudko, Proceedings of 1977 IEEE/OSA Conference on Laser Engineering and Applications, 1977, p. 26.

10. H. Kildal and S. R. J. Brueck, Phys. Rev. Lett. $\underline{38}$, 347 (1977), DDC AD-A042238.

11. S. Ezekiel and R. Weiss, Phys. Rev. Lett. $\underline{20}$, 91 (1968); A. S. Pine, private communication.

12. W. R. L. Clements and B. P. Stoicheff, Appl. Phys. Lett. $\underline{12}$, 246 (1968).

13. R. V. Ambartzumian, Yu. A. Gorokhov, V. S. Letokhov, and G. N. Makarov, JETP Lett. $\underline{21}$, 171 (1975).

14. J. L. Lyman, R. J. Jensen, J. Rink, C. P. Robinson, and S. D. Rockwood, Appl. Phys. Lett. $\underline{27}$, 87 (1975).

15. R. V. Ambartzumian, Tunable Lasers and Applications, A. Mooradian, T. Jaeger, and P. Stokseth, Editors (Springer-Verlag, Berlin, 1976), p. 150.

16. J. I. Steinfeld, J. Burak, D. G. Sutton, and A. V. Nowak, J. Chem. Phys. $\underline{52}$, 5421 (1970).

17. P. F. Moulton, D. M. Larsen, J. N. Walpole, and A. Mooradian, Opt. Lett. $\underline{1}$, 51 (1977).

18. D. S. Frankel, J. Chem. Phys. $\underline{65}$, 1696 (1976).

19. R. D. Bates, J. T. Knudtson, G. W. Flynn, and A. M. Ronn, Chem. Phys. Lett. $\underline{8}$, 103 (1971).

III. MATERIALS RESEARCH

A. EFFECT OF O_2 PRESSURE ON PROPERTIES OF Sn-DOPED In_2O_3 FILMS

Films of Sn-doped In_2O_3 (generally designated as ITO, for indium tin oxide) are useful as transparent conductors in a variety of applications. Recently, for example, such films have been developed as wavelength-selective surfaces for solar collectors[1,2] and as transparent heterojunction layers for photovoltaic solar cells.[3,4] The optical and electrical properties of rf-sputtered ITO films are known to be quite sensitive to preparation conditions. Although films with good transmission and conductivity have been obtained both by deposition at very low Ar gas throughput[5,6] and by post-deposition annealing,[7,8] it has been difficult to achieve satisfactory reproducibility. We have now investigated the effect of the O_2 partial pressure during deposition, $P(O_2)$, on the properties of as-deposited ITO films. For a given set of deposition conditions, we find that high-quality films can be prepared only within a narrow range of $P(O_2)$ values.

The ITO films were obtained by rf-sputtering, in Ar gas, of a 12.7-cm-diameter, hot-pressed target of composition In_2O_3-15 m/o SnO_2. (Two different targets were used.) The sputtering apparatus is a commercial rf diode unit that can easily achieve a base pressure of 5×10^{-7} Torr. (Unless stated otherwise, all pressures are expressed in N_2 equivalents.) The detailed data presented here were obtained for films about 5×5 cm deposited on substrates of Corning CG7059 glass under the following conditions: target-to-substrate distance, 5.7 cm; Ar pressure, 10^{-2} Torr (as measured with a capacitive manometer); Ar flow rate, 20 cm^3 (STP)/ min.; pre-deposition sputtering at 550 W for 15 min., followed by deposition at 550 W for 15 min. At the flow rate used, the Ar throughput was 0.25 Torr-l/sec, much higher than in our previous experiments.[6] During film deposition, the substrate was heated by the electron bombardment intrinsic to rf sputtering. After about 5 min. of deposition at 550 W, the substrate surface temperature reached a steady-state value of about 450 °C, as measured by chromel-alumel thermocouples attached to the surface with kaolin-sodium silicate paste.[6]

Throughout each deposition run, $P(O_2)$ was maintained at a preselected value, in the range from 1×10^{-4} to 1×10^{-5} Torr, by admitting O_2 to the sputtering chamber through a manually controlled leak valve. The value of $P(O_2)$ was continuously monitored by means of a residual gas analyzer (RGA) that was connected to the sputtering chamber through a capillary leak and pumped at a rate sufficient to reduce the total pressure from 10^{-2} Torr, the value in the chamber, to 2 to 3×10^{-5} Torr, close to the maximum operating pressure for the analyzer. A calibration curve for the RGA was determined before each deposition run. The Ar flow was then initiated, the O_2 leak rate adjusted to give the desired $P(O_2)$, and pre-sputtering was begun. In order to keep $P(O_2)$ constant during the run, it was usually necessary to increase the leak rate at the beginning of pre-sputtering, probably because of O_2 uptake by the target, and to decrease the rate from time to time during the remainder of pre-sputtering and during sputtering, probably because of O_2 desorption by the chamber walls and other components.

The electrical resistivity of the ITO films was determined by both four-point-probe and van der Pauw measurements, which gave results agreeing within 10 percent. The Hall coefficient was also measured by the van der Pauw technique. The optical transmission was measured as a function of wavelength from 0.35 to 0.9 μm. Film thickness was determined by using
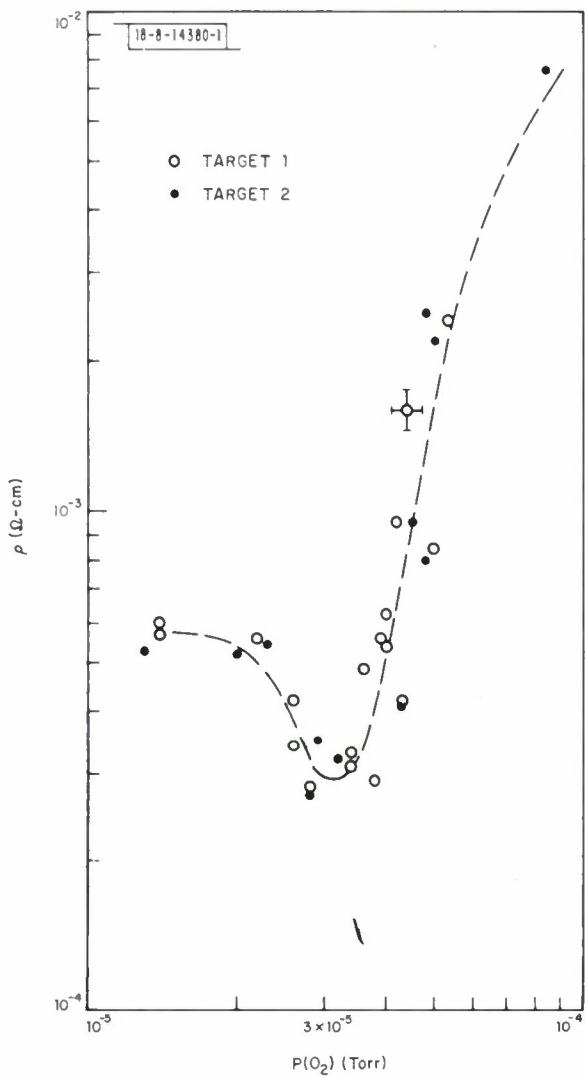
Fig. III-1. Resistivity ρ of rf-sputtered ITO films as a function of O_2 partial pressure during deposition, $P(O_2)$.
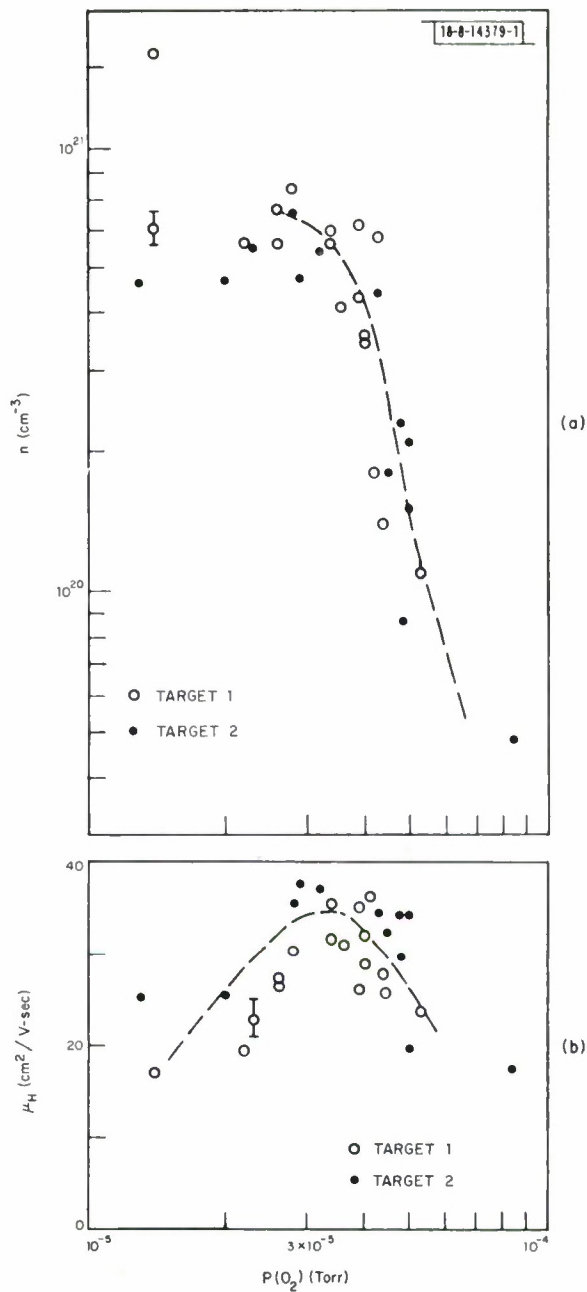
Fig. III-2. (a) Carrier concentration n and (b) Hall mobility μ_H of ITO films as a function of $P(O_2)$.

microtopography to measure the height of steps obtained by etching the film with concentrated HCl heated to 50 °C, which gives an etching rate of ~0.3 μm/min. Most of the films were between 0.5 and 0.8 μm thick.

Figure III-1 shows the electrical resistivity ρ of ITO films, prepared under the conditions specified above, as a function of $P(O_2)$ during deposition. For the lowest pressures used, $P(O_2) \simeq 1.3 \times 10^{-5}$ Torr, ρ is about 6×10^{-4} Ω-cm. With increasing pressure, ρ decreases to a minimum of ~3×10^{-4} Ω-cm at 3 to 4×10^{-5} Torr, then rises sharply. At $P(O_2) = 6 \times 10^{-5}$ Torr, for example, ρ is already about an order-of-magnitude higher than the minimum value. The carrier concentration n and Hall mobility μ_H are plotted against $P(O_2)$ in Fig. III-2(a) and (b), respectively. All the films are n-type. With increasing pressure, n initially remains roughly constant at 5 to 7×10^{20} cm^{-3}, then drops abruptly at about 4×10^{-5} Torr, resulting in the sharp increase observed in ρ. The mobility exhibits a shallow maximum of ~35 cm^2/V-sec at 3 to 4×10^{-5} Torr. This maximum accounts for the minimum in ρ observed in this pressure region.

The optical transmission (T) of the ITO films, integrated over the 0.45- to 0.80-μm wavelength range and corrected for the attenuation of the glass substrate, is plotted against $P(O_2)$ in Fig. III-3. At the lowest pressures, T is quite low, and the films appear black (as they do if no O_2 is introduced during deposition). With increasing pressure, T at first increases rapidly, exceeding 80 percent at 3×10^{-5} Torr, and then becomes essentially constant at over 90 percent.
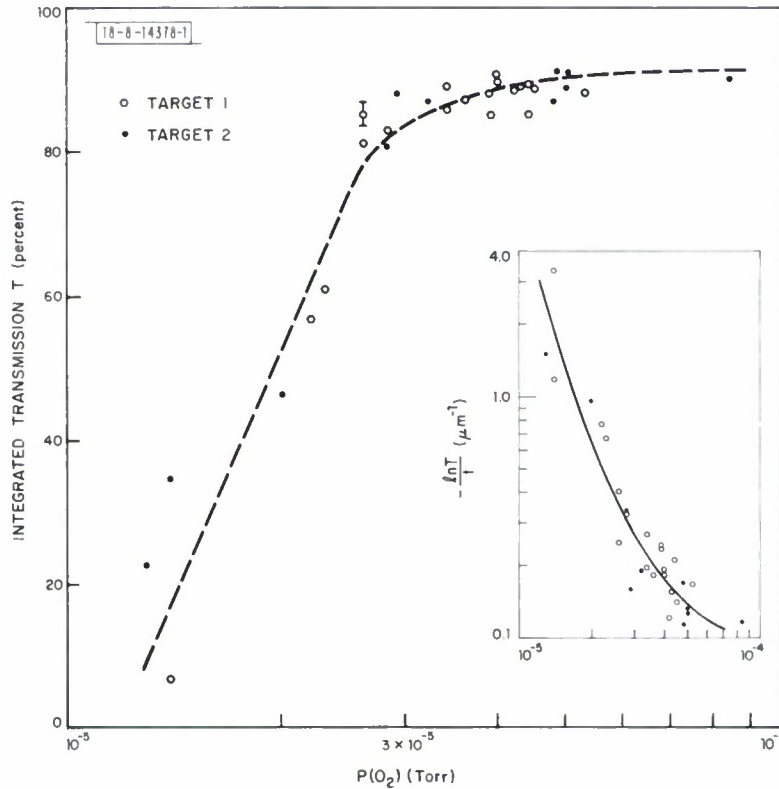
Fig. III-3. Optical transmission T of ITO films, integrated over wavelength range from 0.45 to 0.80 μm, as a function of $P(O_2)$. Inset shows quantity $-(\ln T)/t$, where t is film thickness, plotted against $P(O_2)$.

27

The inset in Fig. III-3 shows the variation with $P(O_2)$ of the quantity $-(\ln T)/t$, where t is the film thickness. For low values of T, this quantity is roughly proportional to the average absorption coefficient α over the wavelength range measured. Since the reflectivity of the films is 0.10 to 0.15 over this wavelength range, the values of $-(\ln T)/t$ obtained at the lowest O_2 pressures correspond to values of α as high as 3×10^4 cm^{-1}. The decrease in $-(\ln T)/t$ with increasing $P(O_2)$ corresponds to a monotonic decrease in α. At the highest values of $P(O_2)$, the absorption of the films between 0.45 and 0.80 μm is so low that the transmission is essentially reflectivity-limited, making it difficult to obtain accurate values of α.

In addition to increasing the visible transmission of the films, increasing $P(O_2)$ during deposition results in a shift of the intrinsic absorption edge to longer wavelengths (i.e., lower photon energies). This shift is due to the decrease in carrier concentration, which lowers the Fermi level and reduces the magnitude of the Burstein effect.[9] Thus, the absorption edge moves from about 3.5 to about 3.0 eV when n decreases from 6×10^{20} to 1×10^{20} cm^{-3}.

X-ray diffractometer measurements were used to obtain diffraction patterns for a number of the ITO films. All the lines in the patterns can be assigned to the cubic bixbyite[10] structure of In_2O_3, but the lattice constant values are larger than the value for bulk, undoped In_2O_3 ($a_o = 10.118$ Å), and they depend on $P(O_2)$. For the lowest values of $P(O_2)$, $a_o \simeq 10.15$ Å, while for $P(O_2) \geqslant 5 \times 10^{-5}$ Torr, $a_o \simeq 10.23$ Å. The patterns for films deposited at intermediate pressures consist of lines corresponding to both of these a_o values, indicating the presence of two cubic phases. Over the whole pressure range, the films have either ⟨111⟩ or ⟨100⟩ preferred orientation. Their electrical and optical properties appear to be independent of orientation.

Although the x-ray diffraction results do not establish a detailed mechanism for the reduction in optical quality of the ITO films deposited at low values of $P(O_2)$, they do indicate a correlation between low visible transmission and the presence of the cubic phase with $a_o \simeq 10.15$ Å. We have previously suggested that the darkening of ITO films might be due to the formation of an Sn_3O_4-like phase. The x-ray data provide no evidence for such a phase in any of the films examined in this investigation. (However, the data do not eliminate the possibility that a phase of this type might be present in a form or at a concentration level not detected by our diffraction measurements.)

Comparison of Figs. III-1 and III-3 shows that, for the particular deposition conditions used, ITO films with both high electrical conductivity and high visible transmission were obtained only over a very narrow range of $P(O_2)$ values, from 3×10^{-5} to 4×10^{-5} Torr. The properties of the films prepared within this range are comparable to the best previously reported.[5,6,8] In less detailed studies of films deposited at other rf power levels, we found that the $P(O_2)$ ranges yielding high conductivity and transmission, although different, were no wider. These observations appear to explain the difficulties that have previously been encountered in obtaining high-quality ITO films, and they show that close control of the O_2 partial pressure during deposition is essential for reproducible preparation of such films for use as transparent conductors in optoelectronic devices.

J. C. C. Fan
F. J. Bachner
G. H. Foley

B. CHEMISORBED PHASES OF H_2O ON TiO_2 AND $SrTiO_3$

The successful use of the transition-metal oxides TiO_2 (rutile) and $SrTiO_3$ as catalytic electrodes in the photo-assisted decomposition of H_2O (photoelectrolysis) has stimulated recent

experimental investigations of their surface electronic properties.[11-13] For both materials, the Ti ions of stoichiometric, nearly perfect surfaces are found to have essentially the same electronic configuration as bulk Ti ions, $Ti^{4+}(3d^0)$, while defects produced by ion bombardment create a band of d-electron surface states associated with surface $Ti^{3+}(3d^1)$ ions.[11,12] We have now used ultraviolet photoemission spectroscopy (UPS) to investigate the interaction of H_2O with TiO_2 and $SrTiO_3$ surfaces at room temperature.

The surfaces studied were reduced, Ar-ion-bombarded $TiO_2(110)$ and $SrTiO_3(100)$, both before and after annealing. The bombarded surfaces are disordered and nonstoichiometric (O-deficient for TiO_2, O- and Sr-deficient for $SrTiO_3$). Annealing of bombarded $TiO_2(110)$ restores both the atomic order and the stoichiometry, removing the d-electron surface states,[11] while annealing of bombarded $SrTiO_3(100)$ produces an ordered surface (exhibiting good LEED patterns) that is still O- and Sr-deficient and retains its d-electron surface states.[12] UPS measurements were made on the various surfaces before and after exposing them to H_2O vapor.

Figure III-4 shows some of the spectra obtained for an initially clean, ion-bombarded $TiO_2(110)$ surface after successive exposures to H_2O. The number of emitted electrons n(E)
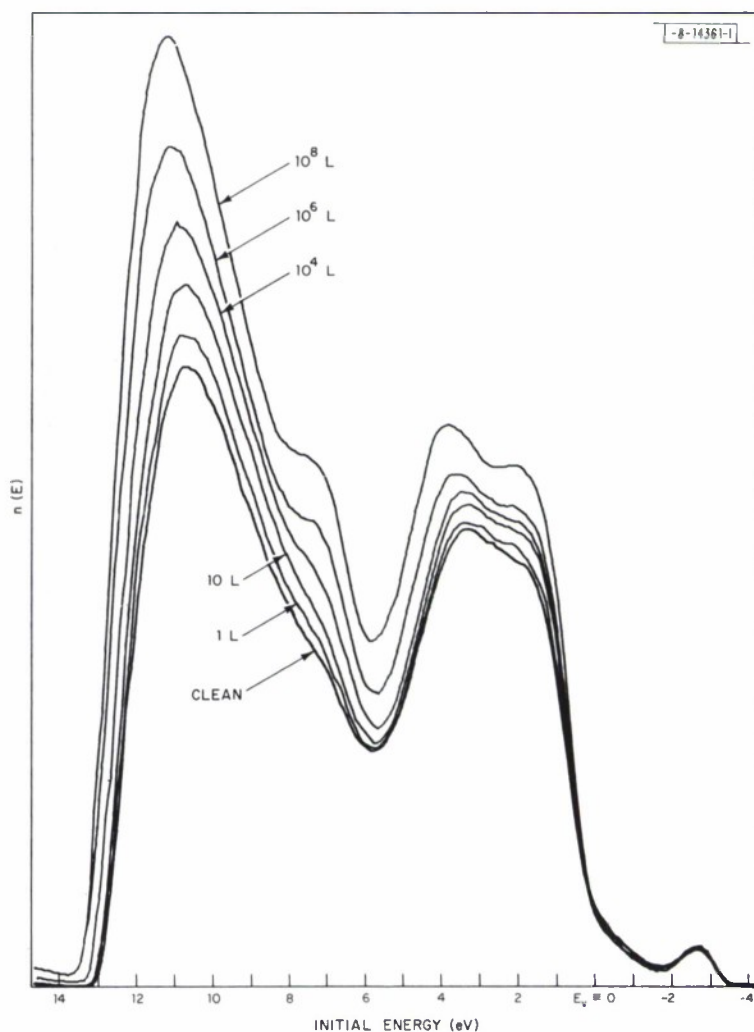
Fig. III-4. He(I) photoemission spectra of initially clean, argon-ion-bombarded $TiO_2(110)$ surface after successive exposures to H_2O ($h\nu$ = 21.2 eV).
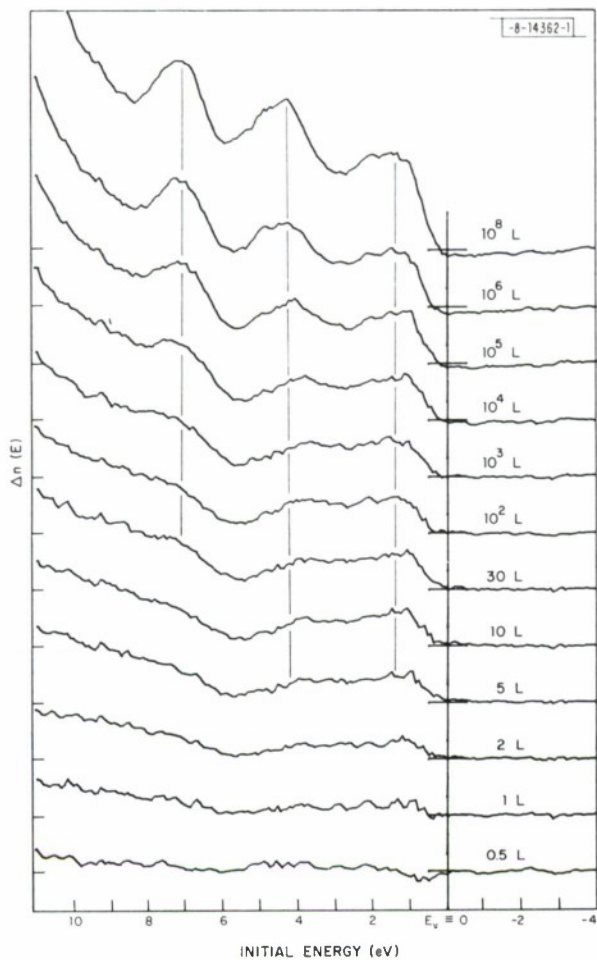
Fig. III-5. He(I) photoemission difference spectra of initially clean, argon-ion-bombarded $TiO_2(110)$ surface after successive exposures to H_2O (hν = 21. 2 eV).
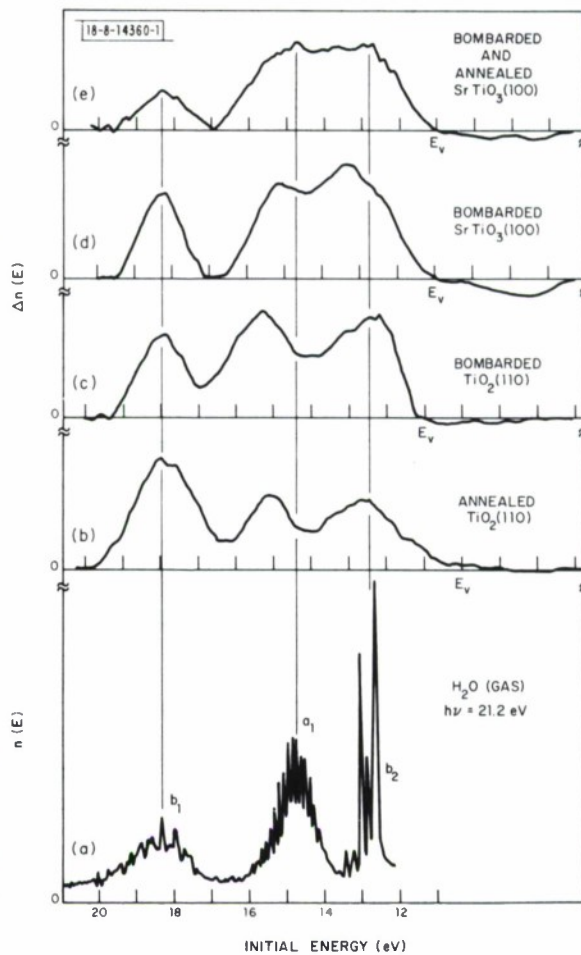
Fig. III-6. He(I) photoemission spectrum of gaseous H_2O compared with He(I) photoemission difference spectra of TiO_2 and $SrTiO_3$ after exposure to 10^8 L of H_2O.

is plotted vs their initial-state energy, measured from the upper edge of the valence band E_v. The peak at about 3 eV above E_v is due to the surface states associated with surface Ti^{3+} ions (1 to 2 per surface unit cell). Figure III-4 shows that exposure to H_2O increases the amplitude of the spectra below E_v but does not affect the surface-state emission.

In order to show the changes in the UPS signals resulting from H_2O adsorption, difference spectra were obtained for each run by subtracting the spectrum for the clean surface from each of the spectra measured after successive H_2O exposures. For weak adsorbate-substrate interactions, such difference spectra can be compared with the UPS spectrum of the adsorbate molecule in the gas phase.[14] All the difference spectra obtained for the run on ion-bombarded $TiO_2(110)$ are plotted in Fig. III-5 (the measured spectra were aligned at E_v before taking differences).

Two types of spectra are seen in Fig. III-5. For exposures up to 10 L (where 1 L = 10^{-6} Torr-sec), two peaks, separated by 2.5 eV, occur in the region of the valence band (0 to ~6 eV). For exposures greater than 30 L, a third peak appears about 7 eV below E_v and grows until at 10^8 L a distinct three-peaked spectrum similar to that of the gas-phase H_2O molecule[15] is obtained. The two-peaked initial spectrum is due to an adsorbed phase with a sticking coefficient of 0.2 to 0.5. This spectrum is seen for both ion-bombarded and annealed $TiO_2(110)$ surfaces, but not for $SrTiO_3(100)$ surfaces, which yield three-peaked spectra even for small H_2O exposures. We believe that the two-peaked structure is due to OH radicals produced by dissociative chemisorption of H_2O. This model is supported by recent measurements of the UPS spectrum for the OH radical in the gas phase, which indicate two bands with ionization potentials of 13.01 and 15.20 eV (Ref. 16), and also by infrared absorption spectra showing that OH is a stable species on TiO_2 (Ref. 17). If the adsorbed species is OH, comparison of the difference spectrum with the free OH spectrum gives a polarization-relaxation (P-R) shift close to that found for molecular H_2O from the data for higher exposures (see below). The fact that $SrTiO_3$ surfaces exhibit only three-peaked difference spectra indicates that dissociative chemisorption of H_2O does not occur on these surfaces.

For the four types of surfaces we have studied, the UPS difference spectra obtained after an H_2O exposure of 10^8 L are shown in Fig. III-6 along with the UPS spectrum for gas-phase H_2O measured for the same photon energy.[15] (A smooth background has been subtracted from the difference spectra to facilitate peak location.) Each of the difference spectra has three peaks with spacings similar to those of the peaks in the gas-phase spectrum, which are due to the b_1, a_1, and b_2 orbitals of H_2O. We conclude that chemisorption at large H_2O exposures is nondissociative. Therefore, quantitative comparison between the difference and gas-phase spectra can yield information concerning the perturbation of the H_2O molecule due to adsorption. In making such a comparison, the difference spectrum is first shifted sufficiently with respect to the gas-phase spectrum to align one or more of the peaks in the two spectra according to some assumption concerning bonding effects in adsorption. The shift gives the amount by which the binding energy of the molecule is reduced on adsorption, the P-R shift.[14] Any remaining differences between the spectra are then attributed to specific bonding effects. The P-R shifts found for the surfaces studied here are given in Table III-1, along with the work functions of the clean and H_2O-covered surfaces.

For both TiO_2 surfaces, the outer two peaks in the difference spectra can be very nearly aligned with the peaks for the b_1 and b_2 orbitals of the gaseous H_2O molecule. The a_1 orbital, however, is shifted toward tighter binding by about 1.0 eV on the bombarded surface and 0.7 eV on the annealed surface. These results support the assumption that bonding effects are not

TABLE III-1

WORK FUNCTIONS AND POLARIZATION-RELAXATION SHIFTS FOR H_2O ON TiO_2 AND $SrTiO_3$
(Energies in eV)

	Φ_{clean}	Φ_{H_2O}	$\Delta\Phi_{H_2O}$	P-R Shift
Bombarded $TiO_2(110)$	5.06	4.56	−0.50	3.6
Annealed $TiO_2(110)$	5.32	4.88	−0.44	2.5
Bombarded $SrTiO_3(100)$	2.79	3.80	1.01	3.7
Bombarded-ond-Anneoled $SrTiO_3(100)$	3.15	4.05	0.90	3.7

important for the b_1 and b_2 levels. Thus, the strongest interaction with the substrate occurs with the a_1 orbital, the O lone-pair orbital in the plane of the H_2O molecule, the interaction being stronger on defect surfaces. The increased binding of the a_1 orbital suggests that the molecule is oriented with the O atom toward the surface. The fact that the energies of the b_1 and b_2 orbitals relative to each other are unchanged on adsorption further suggests that the symmetry axis of the molecule is nearly normal to the surface.

For the bombarded-and-annealed $SrTiO_3(100)$ surface, all three peaks in the difference spectrum have the same relative energies as in the gas-phase H_2O spectrum, indicating a weak adsorbate-substrate interaction. In this case, there is only a small decrease in the emission from the d-electron surface states. For the bombarded $SrTiO_3(100)$ surface, the spacing between the a_1 and b_2 orbital peaks in the difference spectrum is the same as in the gas-phase H_2O spectrum, but the b_1 orbital is 0.5 eV closer to the a_1 and b_2 orbitals. In Fig. III-6(d) we have aligned the b_1 orbital with that of the free H_2O molecule, on the assumption that this orbital is least likely to be perturbed on adsorption. Thus, the a_1 and b_2 orbitals are both shifted 0.5 eV toward tighter binding. This suggests a more complicated orientation of the H_2O molecule than on TiO_2, with the O lone-pair orbital normal to the plane of the molecule (the b_2 orbital) also involved in the bonding. Similar shifts have been seen for CH_3OH adsorbed on Ni and Ru (Ref. 18). The d-electron surface states on bombarded $SrTiO_3$ are unaffected by H_2O up to 10^6 L; at 10^8 L, however, they become almost completely depopulated, as indicated by the negative dip in Fig. III-6(d) about 3 eV above E_v.

The P-R shifts listed in Table III-I exhibit an interesting dependence on the presence of d-electron surface states. The bombarded $TiO_2(110)$ and both $SrTiO_3(100)$ surfaces, which have filled $Ti^{3+}(3d^1)$ surface states, give similar shifts (3.7 ± 0.2 eV), even though their work functions before H_2O exposure differ by as much as 2.3 eV. The annealed $TiO_2(110)$, which

has no surface Ti^{3+} ions, gives a smaller shift. This difference indicates that, even when there is no charge transfer between the surface states and the adsorbed H_2O molecules, these states have a pronounced effect on P-R of the molecules.[14]

V. E. Henrich
G. Dresselhaus
H. J. Zeiger

C. HIGH Na^+-ION CONDUCTIVITY IN $Na_5YSi_4O_{12}$

Solid electrolytes with high Na^+-ion conductivity are needed for use in high-energy-density secondary batteries such as the Na-S battery now under development. The essential structural feature of such superionic conductors is a rigid, three-dimensional network having an interstitial space that is interconnected in at least one dimension and partially occupied by mobile Na^+ ions. The most extensively investigated of these materials is Na-β-alumina, which has a conductivity of about 0.4 Ω^{-1} cm^{-1} at 300°C. We recently reported[19] the discovery of a new superionic conductor, $Na_3Zr_2Si_2PO_{12}$ (NASICON), that has the same conductivity at 300°C as Na-β-alumina but has several potential advantages as a ceramic material. In NASICON the three-dimensional network is composed of ZrO_6 octahedra, SiO_4 tetrahedra, and PO_4 tetrahedra. In an attempt to find new solid electrolytes, we have extended our investigation to other systems with both octahedra and tetrahedra. We have found that $Na_5YSi_4O_{12}$ (Ref. 20), in which the network contains YO_6 octahedra and SiO_4 tetrahedra, also exhibits high ionic conductivity — about 0.1 Ω^{-1} cm^{-1} at 300°C.

To synthesize $Na_5YSi_4O_{12}$, a mixture of Na_2CO_3, Y_2O_3, and SiO_2 in a molar ratio of 5:1:8 was placed in a platinum crucible and heated overnight in air at 1100°C. A cylindrical specimen was formed by mixing the reaction product with polyethylene glycol binder, isostatically pressing at 60,000 psi, and sintering for 3 hr in air at 1190°C. The cylinder obtained was 19.8 mm long and 5.8 mm in diameter with a density of 2.63 g/cm^3, 92 percent of the theoretical density. Resistance measurements using pseudoreversible graphite dag electrodes were made at 200°, 250°, and 300°C on the full-length cylinder and on samples 12.9 and 6.6 mm long obtained by cutting the cylinder in two. For each temperature, the data for resistance as a function of sample length fit a straight line, which can be extrapolated to zero length to give the electrode resistance. The sample resistance values corrected by subtracting the electrode contribution yield conductivity (σ) values of 0.05, 0.07, and 0.10 Ω^{-1} cm^{-1} at 200°, 250°, and 300°C, respectively. The quantity $\log(\sigma T)$, where T is the absolute temperature, is plotted against $1/T$ in Fig. III-7.
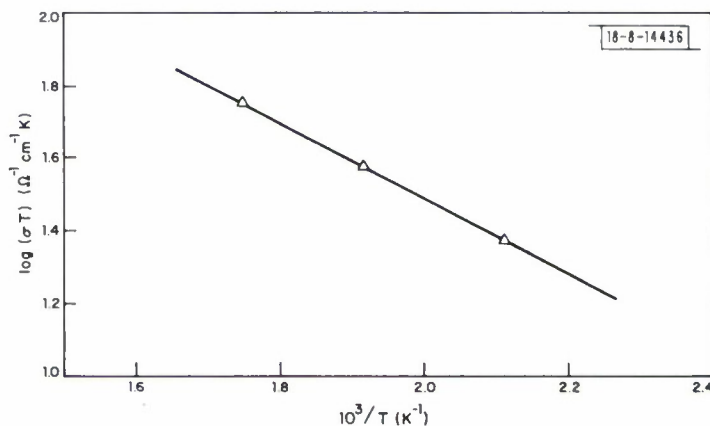

Fig. III-7. Logarithm of product of conductivity σ and absolute temperature T for $Na_5YSi_4O_{12}$ as a function of $1/T$.

The points fit a straight line whose slope corresponds to an activation energy of 0.20 eV, compared with 0.16 and 0.24 eV for Na-β-alumina and NASICON, respectively.

Specimens of $Na_5YSi_4O_{12}$ more closely approaching the theoretical density (2.86 g/cm^3, compared with 3.25 to 3.27 g/cm^3 for Na-β-alumina and NASICON) might be expected to have still higher conductivity values than those reported here. Even the present values are high enough, coupled with the material's relative ease of synthesis and sintering, to justify further investigation of $Na_5YSi_4O_{12}$ as a promising solid electrolyte for battery applications.

H. Y-P. Hong

REFERENCES

1. R. B. Goldner and H. M. Haskal, Appl. Opt. 14, 2328 (1975); R. B. Goldner, Appl. Opt. 16, 808 (1977).

2. J. C. C. Fan, F. J. Bachner, and R. A. Murphy, Appl. Phys. Lett. 28, 440 (1976), DDC AD-A027110/6; J. C. C. Fan and F. J. Bachner, Appl. Opt. 15, 1012 (1976), DDC AD-A027105/6.

3. J. B. DuBow, D. E. Burk, and J. R. Sites, Appl. Phys. Lett. 29, 494 (1976).

4. K. S. SrceHarsha, K. J. Bachman, P. H. Schmidt, E. G. Spencer, and F. A. Thiel, Appl. Phys. Lett. 30, 645 (1977).

5. D. B. Fraser and H. D. Cook, J. Electrochem. Soc. 119, 1368 (1972).

6. J. C. C. Fan and F. J. Bachner, J. Electrochem. Soc. 122, 1719 (1975), DDC AD-A024234/7.

7. R. R. Mehta and S. F. Vogel, J. Electrochem. Soc. 119, 753 (1972).

8. J. A. Thornton and V. L. Hedgcoth, J. Vac. Sci. Technol. 13, 117 (1976).

9. E. Burstein, Phys. Rev. 93, 632 (1954).

10. R. W. G. Wyckoff, Crystal Structures (Wiley, New York, 1964), Vol. 2, 2nd Edition, p. 2.

11. V. E. Henrich, G. Dresselhaus, and H. J. Zeiger, Phys. Rev. Lett. 36, 1335 (1976), DDC AD-A030621.

12. _____, Bull. Am. Phys. Soc. Ser. II 22, 364 (1977).

13. M. L. Knotek and J. E. Houston, Phys. Rev. B 15, 4580 (1977).

14. J. E. Demuth and D. E. Eastman, Phys. Rev. Lett. 32, 1123 (1974).

15. D. W. Turner, C. Baker, A. D. Baker, and C. R. Brundle, Molecular Photoelectron Spectroscopy (Wiley-Interscience, New York, 1970), p. 113.

16. S. Katsumata and D. R. Lloyd, Chem. Phys. Lett. 45, 519 (1977).

17. See, for example, F. Gonzalez and G. Munuera, Revue de Chimie Minerale 7, 1021 (1971), and references therein.

18. G. W. Rubloff and J. E. Demuth, J. Vac. Sci. Technol. 14, 419 (1977); G. B. Fisher, E. T. Madey, B. J. Waclawski, and J. T. Yates, Proc. 7th Intl. Vac. Congr. and 3rd Intl. Conf. on Solid Surfaces, Vienna, 1977 (to be published).

19. H. Y-P. Hong, Mater. Res. Bull. 11, 173 (1976), DDC AD-A024176/0.

20. B. A. Maksimov, Yu. A. Kharitonov, and N. V. Belov, Sov. Phys.-Doklady 18, 763 (1974).

IV. MICROELECTRONICS

A. HIGH-EFFICIENCY GaAs SHALLOW-HOMOJUNCTION SOLAR CELLS

High-efficiency GaAs single-crystal solar cells have been fabricated without the use of $Ga_{1-x}Al_xAs$ layers. These devices utilize a homojunction formed by chemical vapor deposition (CVD) of a thin n^+ layer on a thicker p layer. For antireflection-coated cells 1×0.5 cm in area, the highest measured conversion efficiency so far obtained is 15.3 percent (17 percent when corrected for contact area) at AM 1 (unity air mass). These efficiencies are approaching those obtained with $Ga_{1-x}Al_xAs/GaAs$ heterostructures,[1,2] and are considerably higher than those previously reported for homojunction solar cells.[3]

Although conversion efficiencies of 25 to 28 percent at AM 1 are predicted for GaAs p-n junction solar cells under idealized conditions,[4] the maximum efficiency obtained for previous homojunction cells is only 13 to 14 percent at AM 1 (Ref. 3). The reduction in efficiency results primarily because GaAs has a high surface recombination velocity and also has high absorption coefficients[5] for above-bandgap photon energies, with half the carriers due to AM 1 radiation being generated within 0.2 μm of the surface. Consequently, most of the carriers in these cells recombine before they reach the junction, causing a strong decrease in collection efficiency.

Since the recombination velocity is much less at a $Ga_{1-x}Al_xAs/GaAs$ interface than at a GaAs surface, conversion efficiencies as high as 22 percent at AM 1 (Ref. 2) have been achieved for cells in which the top GaAs surface is coated with a thin window layer of $Ga_{1-x}Al_xAs$ grown by liquid phase epitaxy. For fabrication of low-cost solar cells it appears advantageous to grow epitaxial layers by CVD, a process which probably can be scaled up more easily than LPE for large-volume production. However, aluminum is so reactive in the vapor phase that it is difficult to prepare high-quality $Ga_{1-x}Al_xAs$ by conventional CVD, although cells with $Ga_{1-x}Al_xAs$ layers grown by metal-organic CVD have just been reported.[6] According to theoretical calculations,[4] losses in homojunction GaAs cells due to surface recombination can be greatly reduced by making the p-n junction so shallow that most of the carriers are generated below the junction. In the present investigation, we have demonstrated this principle by using CVD to prepare high-efficiency cells with a thin $n^+/p/p^+$ structure in which most of the carriers are generated in the p layer, and the p/p^+ interface provides an electric field that further increases collection efficiency. This structure was adopted in preference to a thin $p^+/n/n^+$ structure because the minority carrier diffusion length in GaAs is greater for electrons than for holes.[7]

The GaAs layers used for the solar cells were grown in an $AsCl_3$-Ga-H_2 CVD system[8] on p^+, Zn-doped, (100)-oriented GaAs substrates with a carrier concentration of 10^{18} cm^{-3}. A p layer 1.7 μm thick was first grown on the substrate, followed by a thin n^+ layer. The p layer ($p < 10^{16}$ cm^{-3}) and n^+ layer ($n \sim 4 \times 10^{18}$ cm^{-3}) were doped with Zn and S, respectively, by using $(C_2H_5)_2$Zn and H_2S sources. The sheet resistance of the n^+ layer was 70 Ω/□. To determine the thickness of this layer, the I-V characteristic between two ohmic contacts to the layer was measured while a channel was being etched between the contacts. When the I-V characteristic for back-to-back diodes was observed, etching was stopped, and the channel depth was measured with a profilometer. The n^+-layer thickness measured by this technique was 1300 Å for the highest efficiency cells.
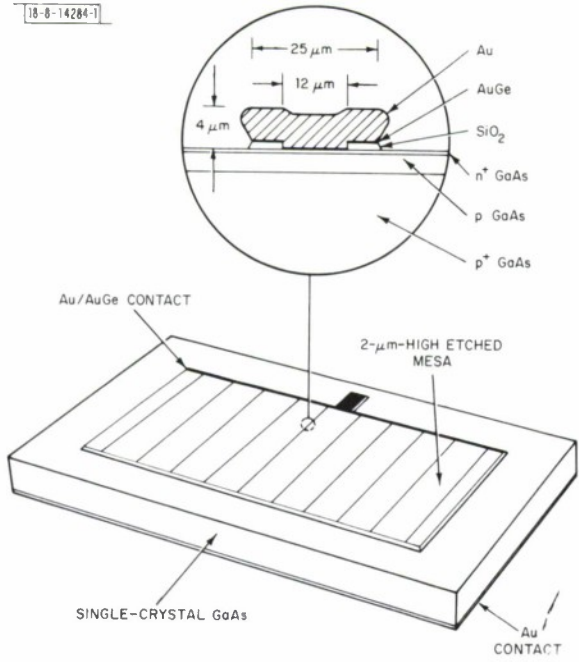
Fig. IV-1. Diagram of single-crystal GaAs shallow-homojunction solar cell. Expanded view shows cross section of a contact finger before deposition of antireflection-coating.

S-doped n$^+$ layer is 1300 Å thick; Zn-doped p layer is 1.7 μm thick.

Fig. IV-2. Quantum efficiency as a function of wavelength for antireflection-coated GaAs solar cell with 15.3-percent conversion efficiency at AM 1.
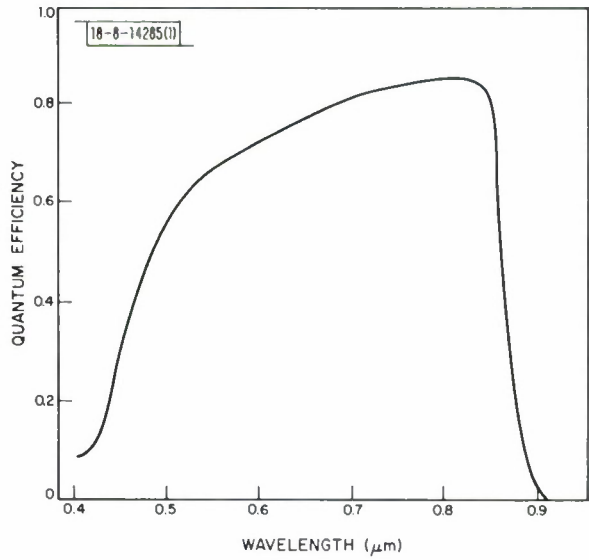
The initial fabrication step following layer growth was the pyrolytic deposition of SiO_2 glass (1000 Å) on the GaAs wafer at 400°C to protect the n^+ layer during the succeeding steps. Openings for ohmic contact fingers were etched in the glass coating using photolithographic techniques. For each cell there were 10 openings, 5 mm long and 12 μm wide, spaced 1 mm apart. The wafer was sputter-etched to remove GaAs to a depth of 50 Å in the finger openings, then sputter-coated with successive layers of Au-12%Ge (300 Å) and Au (2000 Å). The Au/AuGe film was defined photolithographically into 25-μm-wide interconnected fingers that overlaid the openings in the glass. All the photolithographic steps were carried out with standard equipment used for silicon-wafer processing. The wafer was then momentarily annealed (~1 sec) under flowing N_2 at 300°C on a graphite heater strip to establish ohmic contact between the AuGe fingers and the n^+ layer, as verified by measurements of test contacts on the wafer. The conventional technique of alloying at 450°C was not used because it was found to cause penetration of the n^+ layer.

The contact fingers to the n^+ layer were next electroplated with Au to a thickness of 4 μm. The back contact to the p^+ substrate was made with sputtered Au. The active area of the cell was defined by etching a 1- × 0.5-cm rectangular mesa in the GaAs, and the glass layer was removed with buffered HF. A diagram of the cell at this stage, with an expanded cross section of one of the fingers, is shown in Fig. IV-1. Finally, the cell was antireflection-coated with successive layers of SiO (700 Å) and MgF_2 (1200 Å). For GaAs with this two-layer coating, the average reflectivity, measured over the wavelength region 0.5 to 0.9 μm, was less than 5 percent.

Efficiency measurements on the cells were made by using a high-pressure Xe lamp with a water filter as a simulated AM 1 solar source. The incident intensity was adjusted to 100 mW/cm^2 using a NASA standard Si solar cell calibrated for AM 1 as a reference. For our best cell, the open-circuit voltage is 0.91 V, the short-circuit current is 10.3 mA, and the fill factor is 0.82, giving a measured conversion efficiency of 15.3 percent. When the contact area is subtracted, the corrected efficiency is 17 percent. Independent measurements at NASA Lewis Research Center also gave an efficiency of 15.3 percent. The n factor at 100 mA/cm^2 is 1.25, as obtained from the dark I-V characteristics, indicating good material quality with long carrier diffusion lengths.[4] The series resistance is 0.5 Ω.

The quantum efficiency of this cell as a function of wavelength is shown in Fig. IV-2. The quantum efficiency is highest at the longer wavelengths, with a gradual decrease at shorter wavelengths. Since the shorter-wavelength light is absorbed nearer the surface, this suggests that there is still a significant reduction in efficiency due to surface recombination. If so, the use of even thinner n^+ layers should increase the efficiency still further.

Our results demonstrate that homojunction GaAs solar cells with efficiencies approaching those of $Ga_{1-x}Al_xAs/GaAs$ heterostructure cells can be obtained by using a thin $n^+/p/p^+$ structure. In addition to being useful for single-crystal cells, such a structure prepared by chemical vapor deposition may be applicable in the preparation of low-cost, efficient, polycrystalline GaAs solar cells.

<div align="right">

C. O. Bozler
J. C. C. Fan
</div>

B.   SURFACE-ORIENTED MIXER DIODES

Mixing with a 761-GHz submillimeter-wave laser has been obtained with the small surface-oriented GaAs Schottky-barrier mixer diodes described previously.[9,10] Whereas earlier experiments were made with a 334-GHz carcinotron, the new experimental results were obtained at the higher frequency and, in addition, used new methods of coupling the radiation to the diode.

The first of these methods is similar to that developed for point-contact diodes.[11,12] Each terminal of the surface-oriented diode is connected to a quartz stripline filter structure which is suspended across an overmoded reduced-height N guide. A planar device mounted in this manner has been used to harmonically mix the 82nd harmonic of an X-band klystron with the 761-GHz submillimeter laser signal. The X-band signal was introduced through the IF terminals.
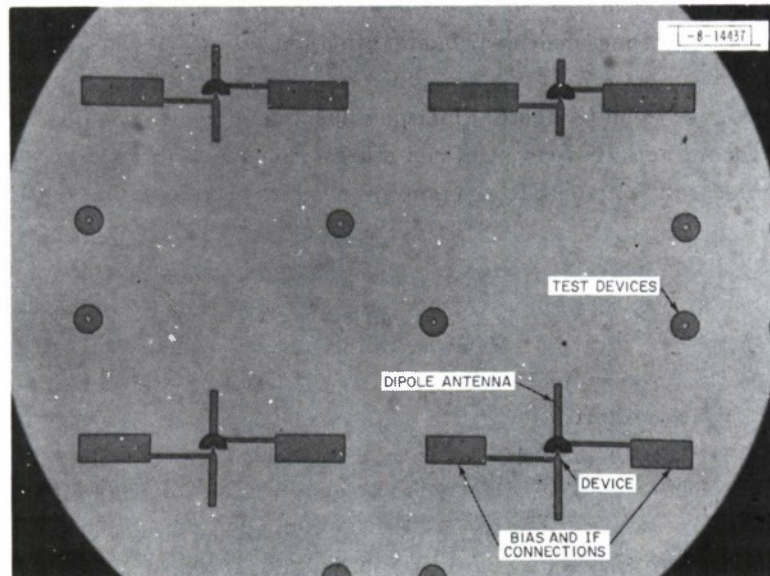
Fig. IV-3. Half-wavelength dipole device structure. Four different sizes of dipoles have been fabricated, having lengths of 0.14, 0.18, 0.22, and 0.25 mm. Annular metallizations are test devices used only in device fabrication.

A second method utilizes integrally connected half-wavelength dipole antennas to enhance the coupling. Figure IV-3 shows devices for four discrete wavelengths which have different lengths of dipole antennas and different dimensions of bias and IF connections. These connections are made to the antenna at low-impedance points near the mixer junction and present a high impedance to the antenna at the design frequencies. The presence of the GaAs dielectric has been taken into account in the calculations of these dimensions.[13] The antenna structures have been tested by suspending them across a hole in a ceramic with an imprinted strip conductor for the bias and IF connections. In these tests, the submillimeter wavelength radiation is focused upon the device, which is backed by an adjustable conducting plane. The response of the diode to this radiation depends quite sensitively upon the position of this plane. Antenna device chips mounted in this configuration have also been used successfully to phase lock, for the first time, our high-frequency carcinotrons directly to stabilized X-band sources. Experiments to determine the specific radiation pattern and frequency sensitivity of these devices are currently in progress.

Antenna device chips are now being used routinely in pulsed heterodyne measurements of high-power D_2O submillimeter lasers at 385 μm and have proved to be mechanically rugged and resistant to RF burnout. Larger arrays of antennas and devices are being designed in

38

order to obtain adequate response without the use of external focusing arrangements for the laser radiation, which will greatly enhance the utility of these devices.

R. A. Murphy   B. J. Clifton
H. A. Fetterman   P. E. Tannenwald
C. D. Parker

C. SUBMICRON GRATING FABRICATION USING CONVENTIONAL PHOTOLITHOGRAPHIC METHODS

Two grating masks consisting of 0.635-μm lines and spaces (788 line pairs/mm) were fabricated for use by the Quantum Electronics Group. These masks were fabricated using conventional photolithographic mask-making apparatus (D. W. Mann Model 1600 A pattern generator and Model 1795 photo-repeater) and represent the achievement of resolution two-times greater than the stated optimized specification for this equipment. The high resolution was achieved by precise processing procedures and by a double-reduction technique which utilized 100X reticles, and photocomposition of 10X reticles and the final mask.

The final grating mask consists of an array of eight 0.838- $\times$ 1.676-mm gratings in a 2 $\times$ 4 matrix. Each grating is separated by 0.025 mm from the adjacent grating. Four of the gratings consist of 0.635-μm equally spaced lines and spaces, with lines oriented parallel to the short side of the grating. The other four gratings differ in that one double-width space (1.27 μm) is created in the center of the grating. The generation of this discontinuity presented a major challenge in the computer layout of this mask and in the photocomposition methods used to expose both the 10X reticle and the final mask. The real measure of success of making a grating of this type can be indicated by the resolution and edge acuity of the lines at the double-space discontinuity compared with those elsewhere in the grating.

An initial attempt was made to fabricate 10X emulsion reticles for each of the two types of gratings. However, because of limitations on the opening of the aperture of the Mann 1600 A pattern generator, linewidth discontinuities of a noticeable 0.2 μm would occur on the final mask. In addition, the edge acuity of the lines will be degraded by multiple reflections from the more than 4000 exposures required per reticle, and exposure limitations in making the contact print that will actually be used as the reticle for the final mask preclude achieving the proper line-to-space ratio on the final mask.

Fortunately, multiple reductions from a pattern generator plate permit the use of the D. W. Mann step-and-repeat camera to make chromium intermediate reticles utilizing photocomposition techniques. Multiple reductions of the linewidth variation from the pattern generator cause variations to be so small as not to be resolved, and full advantage can be made of the Nikkor 28-mm focal-length lens on the repeater.

Because of the difference between the "full grating" array and the grating with the double-width space, two different composition strategies were necessary. For the "full grating," one 100X reticle was generated. Each line consists of 10 butting, 2.5- $\times$ 110-mil rectangles, and the 100X reticle consists of 440 such lines. Misalignments at butting locations of 1 μm for the composition of each line are evident, as in Fig. IV-4, but these will disappear after 100X reduction. Because of the feature sizes, edge acuity and linewidths do not degrade on making the emulsion contact copy which is used to make the 10X reticle.

The 10X reticles for the "full grating" were made by step and repeating 100X reticles on photoresist-coated chromium plates. These plates are coated with 3000 Å of AZ 1350 positive
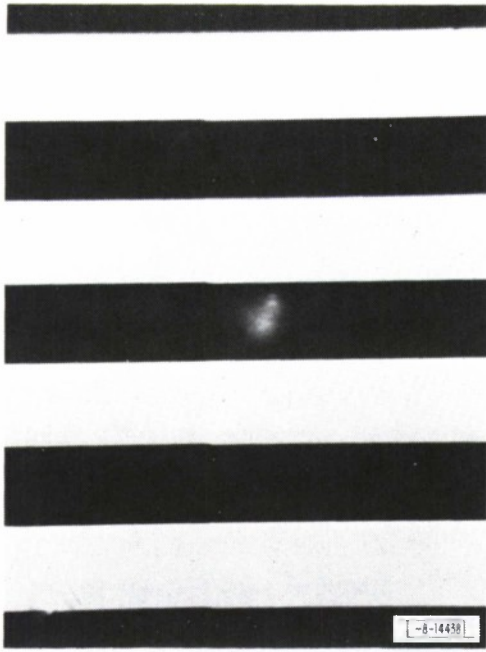
Fig. IV-4. Misalignment at butting locations on 100X reticle. On this emulsion contact print from which 10X reticle will be made, lines and spaces are 2.5 mils wide. Discontinuities in linewidth in center are caused by imprecision in adjustable aperture of D. W. Mann pattern generator. This "jog" amounts to ±1 μm and is particularly noticeable on this reticle, but will be unresolvable after 100X reduction.

Fig. IV-5. Detail of double-width space on 10X "center" reticle. After a 10X reduction on a chromium-plated plate, linewidths are 6.35 μm, with equal size spaces between lines, except double-width space in center. Line discontinuity at butting of photocomposed images is about 0.6 μm. Because of relative size of features, no degradation in line edge acuity can be seen on lines adjacent to double space. Apparent defects seen in this figure are due to dust in inspecting microscope optics.
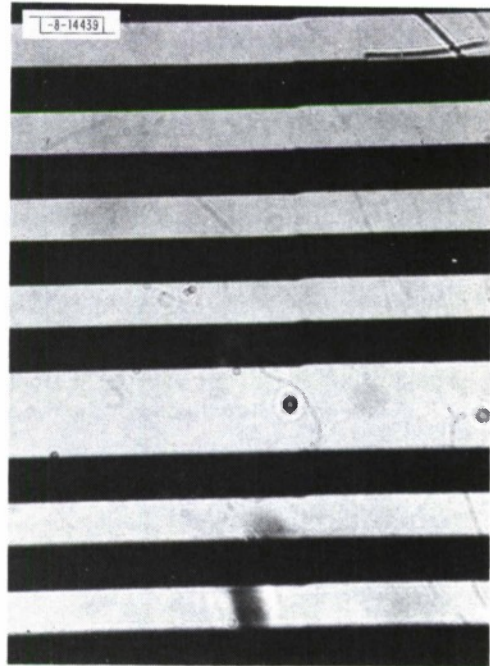
photoresist. The entire reticle is made by photorepeating a 3 × 3 array of the 100X reticle through the 10X reduction lens. The alignment error of the step-and-repeat generator is less than 0.25 μm, and this error will not be resolvable in the final mask. Lines and spaces are both 6.35 μm wide, and the line discontinuity at the butting of the photorepeated images is about 0.6 μm. After photoresist developing and chromium etching, chromium spots in the spaces are removed using a laser mask-corrector which vaporizes the excess chromium. Breaks in the chromium lines cannot be repaired, and 10X reticles with these defects are rejected.

The photorepeated composition of the 10X reticles for the grating with the double-width space is more complex. Three 100X reticles are fabricated. The "left" and "right" reticles are identical to the 100X for the "full grating" except that the "left" 100X reticle is offset by 1.25 mils to the right on the plate. The "right" 100X reticle is a mirror image of the "left" reticle. The "center" reticle is fabricated on the pattern generator such that the two center lines are in contact along their lengths. When the emulsion contact of this 100X reticle is made, a double-width space is in the center as required. The 10X reticle is made by photocomposing a 3 × 3 array on the step-and-repeat camera as discussed above, except that the 3 × 3 array on the reticle consists of a stack of 3 "left," 3 "center," and 3 "right" patterns. This 10X reticle is laser-corrected and used to make the final masks in the same fashion as the "full grating" 10X reticle. Figure IV-5 is a detail micrograph of the 10X "center" reticle. The photocomposition scheme used above is not unique, but it simplifies the mechanics of photocomposing both the 10X and final masks.

The final 1X mask is photocomposed on the repeater using both of the 10X intermediate reticles described above. The final mask consists of 8 gratings in a 2 × 4 array. The four center gratings are made with the double-width space 10X reticle, while the four gratings at the corners of the 2 × 4 array are made with the "full grating" 10X reticle. Spacing between adjacent gratings is 0.025 mm.

The 1X mask is made on a 2- × 2-in. Balzer master grade chromium plate with 900 Å of AZ 1350 positive-working photoresist on 1200-Å chromium. These plates are flat to better than 2 μm over the entire surface. Before exposure, tests were performed to optimize exposure and developing conditions. Using the intensity-compensated 200-W UV lamp in the step-and-repeat machine with the lens at f/2, it was determined that a 1.9-sec exposure coupled with a 15-sec development time optimized the resolution of the resist. The criteria for both exposure and development called for the minimum time needed for equal lines and spaces on the exposed 200- × 200-mil area on the 2 × 2 plate. The developer was a 1:1 solution of AZ developer and water at 21°C and was agitated during development. After development, the masks were rinsed for 2 min. in DI water and blown dry using a low-pressure N_2 stream. Before etching, masks were post-baked at 100°C for 2 hr. Chromium was etched for 100 sec using the standard Transene solution with the mask in a horizontal position. Masks were then cleaned in acetone, ethyl alcohol, and in agitated A-30 stripper at 80°C for 10 min. Ultrasonic cleaning in glass cleaner and DI water was followed by 100-percent microscope inspection.

Four masks were fabricated. The first two suffered from incomplete resist development and were discarded. The final two were acceptable for delivery. The only existing defects were submicrometer breaks in lines, and the best mask had this defect on no more than 2 percent of the area of all eight gratings. Because of the effects of multiple reflections, some edge acuity has been lost on the lines adjacent to the double space, although the definition still is adequate. This reflection problem detracts only slightly from the perfection of the mask, as seen in Fig. IV-6.
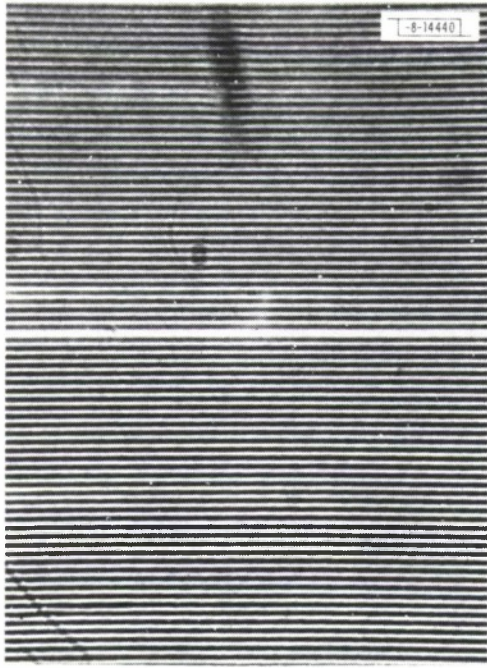
Fig. IV-6. Detail of final mask with double-width space grating. Photomicrograph of center grating region of final masks demonstrates perfection of 0.635-μm lines and spaces. Slight degradation of line acuity resulting from multiple reflections at double-width space in center can be seen. This portion of mask has no line break defects. Apparent "fuzziness" in detail and other "smudges" are due to limitations of inspecting microscope.

In conclusion, gratings of equal 0.635-μm lines and spacings have been fabricated using a double-reduction technique on conventional microelectronic photolithographic mask equipment. By using thin and very uniform AZ resist-coated high-quality chromium-coated plates with calibrated wet chemical techniques, high resolution and good edge acuity are possible. It is essential, however, that all structures on each reticle be of equivalent geometry, and that the final exposure of each reticle on the mask be individually calibrated if reticles differ substantially in pattern.

D. J. Silversmith
G. L. Durant
H. H. Pichler

REFERENCES

1. H. J. Hovel and J. M. Woodall, J. Electrochem. Soc. <u>120</u>, 1246 (1973).

2. J. M. Woodall and H. J. Hovel, Appl. Phys. Lett. <u>30</u>, 492 (1977).

3. H. J. Hovel and J. M. Woodall, <u>12th IEEE Photovoltaic Specialists Conference, 1976</u> (IEEE, New York, 1976), p. 945.

4. H. J. Hovel, <u>Solar Cells</u>, Vol. 11 of <u>Semiconductors and Semimetals</u> (Academic Press, New York, 1975).

5. B. O. Seraphin and H. E. Bennett, <u>Optical Properties of III-V Compounds</u>, Vol. 3 of <u>Semiconductors and Semimetals</u> (Academic Press, New York, 1967).

6. R. D. Dupuis, P. D. Dapkus, R. D. Yingling, and L. A. Moudy, Appl. Phys. Lett. <u>31</u>, 201 (1977).

7. L. W. Aukerman, M. F. Millea, and M. McColl, J. Appl. Phys. <u>38</u>, 685 (1967).

8. Solid State Research Report, Lincoln Laboratory, M.I.T. (1975:2), p. 52, DDC AD-A013103/7.

9. Solid State Research Report, Lincoln Laboratory, M.I.T. (1977:1), p. 32, DDC AD-A041226.

10. R. A. Murphy, C. O. Bozler, C. D. Parker, H. R. Fetterman, P. E. Tannenwald, B. J. Clifton, J. P. Donnelly, and W. T. Lindley, IEEE Trans. Microwave Theory Tech. <u>MTT-25</u>, 494 (1977).

11. Solid State Research Report, Lincoln Laboratory, M.I.T. (1976:4), p. 63, DDC AD-A039175.

12. B. J. Clifton, IEEE Trans. Microwave Theory Tech. <u>MTT-25</u>, 457 (1977).

13. N. Mizuno, Y. O. Daiker, and S. Ono, IEEE Trans. Microwave Theory Tech. <u>MTT-25</u>, 470 (1977).

V. SURFACE-WAVE TECHNOLOGY

A. 310-MHz SAW RESONATOR WITH Q AT THE MATERIAL LIMIT

The combination of a new design approach and a simple fabrication procedure has led to the first realization of a practical surface-acoustic-wave (SAW) two-port resonator with Q at the material limit.[1] In particular, the device on ST quartz exhibited an unloaded Q in excess of 32,000 at 310 MHz when operated in vacuum. The latter value of Q is virtually the same as the best estimate of the material Q at this frequency, which implies that all losses in the system have been rendered negligible in comparison with the intrinsic propagation loss in the material.

Bulk-scattering losses at the edges of the grooved reflection gratings are suppressed by the use of very shallow depths ($\approx$0.01 λ), and leakage losses through the shallow grating are minimized by using a large number (1000) of such grooves.

Bulk-scattering losses from coupling transducers between the gratings are suppressed by taking advantage of a fortuitous match between the material properties of the aluminum used for metallization and the properties of the quartz substrate. When the aluminum fingers of a standard interdigital transducer are recessed into a quartz delay-line surface, surface-wave reflections from the transducers are reduced to a negligible level.[2] Clearly, the discontinuity at a transducer edge is greatly diminished by the recessed geometry, and it is therefore reasonable to expect a corresponding decrease in bulk-wave scattering.

With the above in mind, several two-port SAW resonators incorporating recessed transducers, with cosine apodization for suppression of higher transverse modes,[3] were fabricated in accordance with the sequence shown in Fig. V-1. The photoresist-covered surface of an ST-cut quartz crystal is first exposed to UV light through a mask which contains both the grating and the transducer patterns. (Details of the pattern are given in Table V-1.) Subsequent development results in the entire resonator pattern being defined in the photoresist (Step 1). The crystal is then placed in an ion-beam system for etching of the exposed areas (corresponding to the resonator pattern) to a depth of 1000 Å (Step 2). Following the ion-beam etch, additional photoresist is painted over the (etched) gratings with a brush (Step 3), and the entire surface is then uniformly metallized in an electron-beam deposition system with 100 Å of chrome and 900 Å of aluminum (Step 4). Calculations predict negligible ohmic losses for this thickness of metallization. Finally, the extraneous metal not in the transducer regions is removed by means of the liftoff technique to yield the finished resonator with 1000-Å-deep gratings, and 1000 Å of transducer metallization recessed into the surface (Step 5). Typically, the transducers are flush with the surface to ±100 Å.

Several devices have been made with the above technique. The process is simple, and no difficulties have been encountered. Of the various devices made according to the same nominal specifications of Table V-1, the values of motional resistance R_1 varied between 416 and 488 Ω, and the corresponding unloaded Q's varied between 32,100 and 27,500. The observed variation in parameters is probably due in part to variations in the "surface-wave finish" of the standard-quality crystal blanks employed. A typical wideband (10-MHz) frequency response of these resonators is shown in Fig. V-2(a). It is worthy of note that, as predicted by calculation for the shallow grooves employed, there exists only a single resonance in spite of the relatively

45
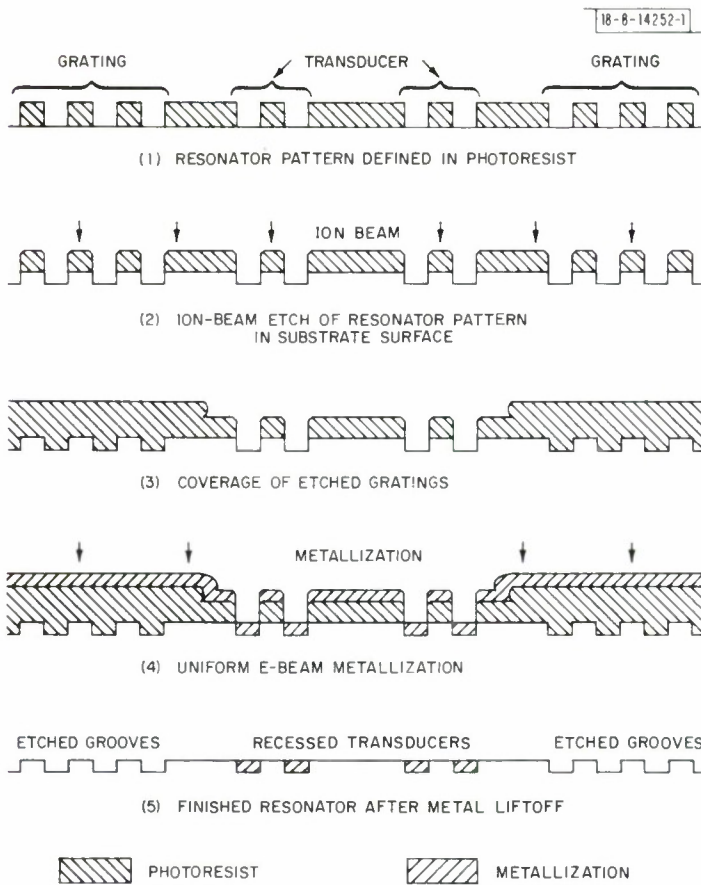
Fig. V-1. Procedure for fabrication of grooved resonator with recessed transducers.

TABLE V-1
DETAILS OF 310-MHz (λ_o = 10 μm) TWO-PORT RESONATOR PATTERN

Grating Aperture	200 λ_o
Grating Period	$\lambda_o/2$
Grating Lines	1000
Grating Separation	100.5 λ_o edge-to-edge
Transducer Finger-Pairs	13.5
Transducer Aperture	100 λ_o
Transducer Apodization	Half-cosine
Finger Width	$\lambda_o/4$

Fig. V-2. Frequency response of 310-MHz two-port SAW resonator on ST quartz in vacuum. (a) Wideband (10-MHz) sweep; (b) narrowband (20-kHz) sweep.
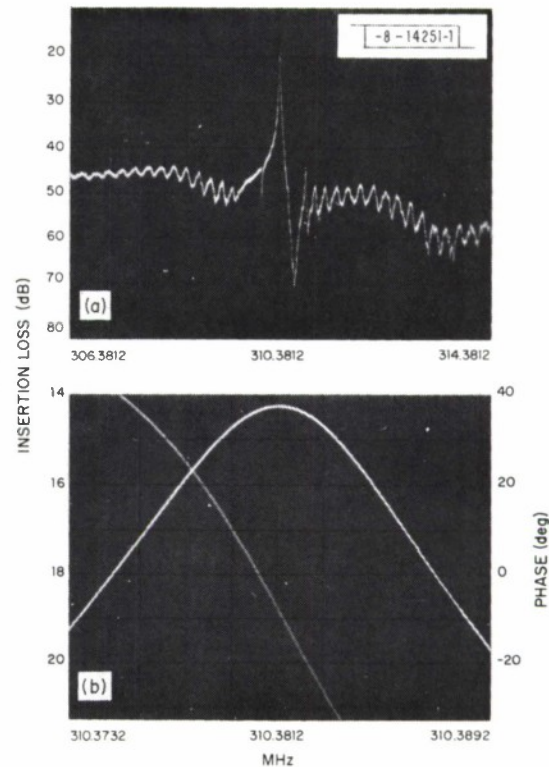
long effective cavity length. An enlargement in the neighborhood of resonance (not shown) would reveal a completely "clean" resonant peak (characteristic of all devices made to date), devoid of "spurs" due to higher transverse modes. Measurements of the 3-dB bandwidth from the expanded-scale plot of Fig. V-2(b) shows the loaded Q to be 25,900. The insertion loss on resonance is 14.3 dB, which corresponds to a resonator series resistance of 416 Ω. Taking into account the 100-Ω loading of the generator and load, the unloaded Q is found to be 32,100.

It is anticipated that the same principles and techniques described above can be applied successfully at frequencies approaching 1 GHz. At much lower frequencies, however, where the material Q is much larger, this technique eventually becomes impractical because of the very long gratings required. Under those conditions, an alternative approach may be to employ the previously described depth tapering[4,5] in conjunction with recessed transducers.

B. ALIGNMENT OF X-RAY-LITHOGRAPHY MASKS USING A NEW INTERFEROMETRIC TECHNIQUE

One of the shortcomings of x-ray lithography has been the absence of a simple method of aligning several separate masks relative to a substrate with a superposition precision of 1000 Å or better. Schemes based on optical moiré techniques[6,7] and two types of x-ray alignment techniques[8-10] have been investigated, but none has been implemented in a practical system. We have developed a new interferometric alignment technique that, in principle, should be capable of aligning masks relative to substrates with a superposition precision less than 100 Å. The technique is compatible with x-ray lithography as well as far-ultraviolet, conformable-photomask, conventional contact and proximity photolithography. Here we will briefly describe the operational features of the technique and show experimental results we have obtained using it to align photomasks and x-ray masks relative to patterns on silicon-wafer substrates.

47
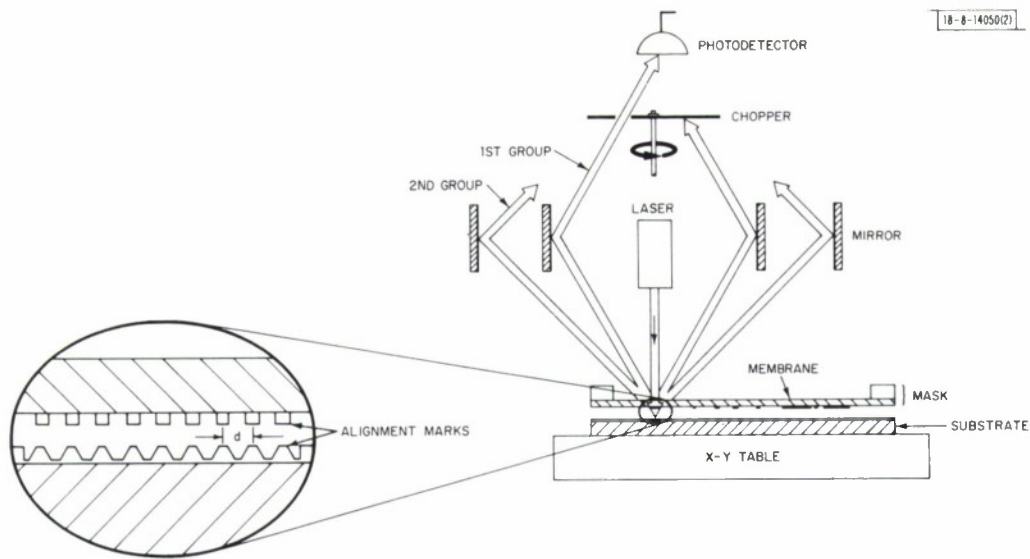
Fig. V-3. Schematic illustration of method used to demonstrate new interferometric alignment technique. Each group consists of two or more constituent beams diffracted by one or both of facing alignment mark gratings. Intensities of symmetrically diffracted groups are measured using photodetector and an oscilloscope. Substrate is aligned by moving it laterally until symmetrically diffracted groups are balanced in intensity.
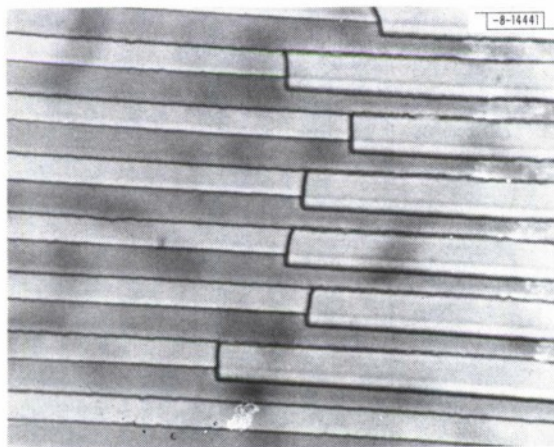
Fig. V-4. Photomicrograph of an exposure following intentional misalignment of a mask grating relative to a grating etched into an SiO$_2$ layer on a silicon wafer substrate. Unevenly broken resist lines are misaligned by about 8500 Å.
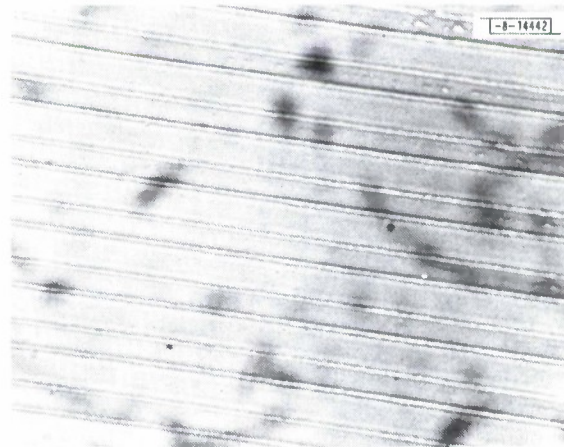

Fig. V-5. Photomicrograph of an experiment identical to that described in Fig. V-4 except that mask and wafer gratings were aligned by balancing intensities of 1st and 3rd groups.

Misalignment is less than 1000 Å.

As described in Ref. 11, a laser or other collimated beam is passed through or reflected from matching alignment marks on masks and wafers. The alignment marks include one or more regular periodic gratings such that gratings of the same spatial period face one another. These gratings give rise to discrete groups of diffracted beams. If the gratings are non-blazed (i.e., structurally symmetric in cross section), alignment or superposition occurs when symmetrically diffracted groups have the same intensity.

Figure V-3 illustrates the simple scheme we used to demonstrate the new interferometric alignment technique. In some cases, photomasks (both 200-μm and 1.5-mm thicknesses) were used in place of the x-ray mask illustrated. Mask and wafer were both mounted on precision X, Y, Z, Θ stages which permitted lateral translation as well as adjustment of the mask-wafer gap and rotation of the wafer. In addition, a special mask-holding fixture allowed adjustment of the mask-wafer parallelism.

The procedure for testing the alignment technique was as follows: A grating was etched into a silicon wafer (or an SiO_2 layer grown on the silicon) either by chemical means or by ion-beam etching. The wafer was then coated with AZ 1350B photoresist or PMMA and mounted on its X, Y, Z, Θ stage. Next, a mask having a grating pattern of the same spatial period as the grating on the wafer, was mounted on its stage, made parallel with the wafer, and then aligned by balancing the intensities of symmetrically diffracted groups. A PIN photodiode was used as the detector, and the group intensities were compared on an oscilloscope. Once mask and wafer gratings were aligned, the resist on the wafer was exposed through the mask. The results shown in Figs. V-4, V-5, and V-6 were obtained with an HeCd laser as the exposure source.

The above procedure was used with gratings in gold on polyimide-membrane x-ray masks[12] having spatial periods of 25, 10, and 1.2 μm. With these gratings we achieved superposition precisions of ~2000 Å, <1000 Å, and ~200 Å, respectively. With 25- and 10-μm gratings, the +1 and −1 groups as well as +3 and −3 groups were balanced. With the 1.2-μm gratings, only +1 and −1 groups exist.
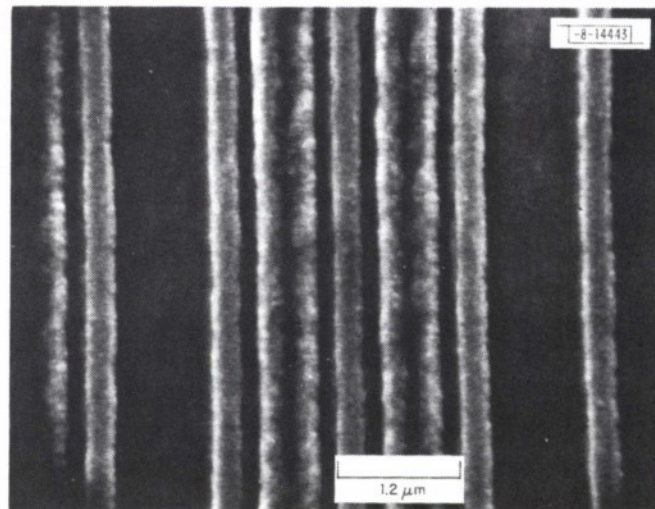
Fig. V-6. Scanning electron micrograph showing results of an experiment in which a 1.2-μm-period gold grating on a polyimide-membrane x-ray mask was aligned relative to a resist-coated grating on an Si substrate and then exposed with an HeCd laser. Alignment precision is estimated to be about 200 Å.

Figure V-4 shows a result obtained with 10-μm-period gratings that were intentionally misaligned such that there was an imbalance in the first groups equal to 13 percent of the maximum observed intensity difference (depth of modulation was approximately 50 percent). The resulting misalignment between the photoresist grating (which appears as unevenly broken lines) and the underlying SiO_2 grating is 8500 Å. Figure V-5 illustrates the alignment achieved by balancing the 1st and 3rd group intensities. Here, the superposition precision of the resist lines relative to the SiO_2 grating is better than 1000 Å.

Figure V-6 is a scanning electron micrograph showing results of an experiment in which a 1.2-μm-period gold grating on a polyimide-membrane x-ray mask was aligned relative to a resist-coated grating on an Si substrate and then exposed with an HeCd laser. Alignment was achieved by balancing the intensities of +1 and −1 diffracted groups. The substrate grating was ion-beam-etched to a depth of about 500 Å, and has a line-to-space ratio <1. The micrograph is of an area where some of the resist lines have lifted up. Substantial diffraction of the HeCd radiation occurred due to the finite mask-substrate gap. The resist lines have recorded this and show some raggedness. Despite this, it is clear that the misalignment is less than 500 Å; we estimate that it is approximately 200 Å.

In our experiments we used alignment marks that consisted of simple periodic gratings of a single spatial period. Obviously, the alignment condition repeats for relative grating displacements equal to the grating spatial period, and thus there is no position of unique superposition. In Ref. 11 we discuss how marks consisting of two gratings having slightly different spatial periods can be used to indicate a unique alignment as well as provide a means for determining the magnitude and direction of misalignment.

The interferometric alignment technique will work over a wide range of mask-sample gaps. Sensitivity to misalignment goes to zero at zero gap as well as any finite gaps where the constituent beams of a group happen to be exactly in-phase with one another. If one wishes to work at such a gap with the particular group, either the laser wavelength or the grating period must be changed to provide adequate sensitivity.

Alignment of masks and wafers in two dimensions is a straightforward extension of the above one-dimensional alignment scheme. It is discussed in some detail in Ref. 13.

We believe that this new interferometric alignment technique solves the alignment problem for x-ray lithography and may be useful in other submicrometer lithographic technologies. Clearly, the technique is not restricted to operate in the optical wavelength region and, in fact, is not restricted to use electromagnetic radiation.

D. C. Flanders
S. Austin
H. I. Smith

REFERENCES

1. R. C. M. Li, "310-MHz SAW Resonator with Q at the Material Limit," Appl. Phys. Lett. (in press).

2. C. Dunnrowicz, F. Sandy, and T. Parker, "Reflection of Surface Waves from Periodic Discontinuities," in 1976 Ultrasonics Symposium Proceedings (IEEE, New York, 1976), p. 386.

3. W. R. Shreve, "Surface-Wave Resonators and Their Use in Narrowband Filters," in 1976 Ultrasonics Symposium Proceedings (IEEE, New York, 1976), p. 706.

4. J. A. Alusow, R. C. M. Li, and R. C. Williamson, paper P-4 of 1976 IEEE Ultrasonics Symposium, Annapolis, MD, 29 September – 1 October 1976.

5. Solid State Research Report, Lincoln Laboratory, M.I.T. (1976:4), pp. 69-71, DDC AD-A039175.

6. M. C. King and D. H. Berry, Appl. Opt. 11, 2455 (1972).

7. J. Schwider and C. Hiller, Opt. Acta 23, 49 (1976).

8. D. L. Spears and H. I. Smith, Solid State Tech. 15, 21 (1972), DDC AD-759257; H. I. Smith, D. L. Spears, and S. E. Bernacki, J. Vac. Sci. Technol. 10, 913 (1973), DDC AD-785092/8.

9. J. H. McCoy and P. A. Sullivan, Solid State Tech. 19, 59 (1976).

10. H. I. Smith, Proc. IEEE 62, 1361 (1974), DDC AD-A006319/8.

11. D. C. Flanders, H. I. Smith, and S. Austin, Appl. Phys. Lett. 31, 426 (1977).

12. D. C. Flanders and H. I. Smith, "Polyimide Membrane X-ray Lithography Masks-Fabrication and Distortion Measurements," edited by G. Varnell, Proc. 14th Symposium on Electron Ion and Photon Beam Technology, Palo Alto, CA, 25-27 May 1977.

13. S. Austin, D. C. Flanders, and H. I. Smith, "Alignment of X-ray Lithography Masks Using a New Interferometric Technique – Experimental Results," edited by G. Varnell, Proc. 14th Symposium on Electron Ion and Photon Beam Technology, Palo Alto, CA, 25-27 May 1977.

REPORT DOCUMENTATION PAGE		READ INSTRUCTIONS BEFORE COMPLETING FORM
1. REPORT NUMBER ESD-TR-77-198	2. GOVT ACCESSION NO.	3. RECIPIENT'S CATALOG NUMBER
4. TITLE *(and Subtitle)* Solid State Research		5. TYPE OF REPORT & PERIOD COVERED Quarterly Technical Summary 1 May – 31 July 1977
		6. PERFORMING ORG. REPORT NUMBER 1977:3
7. AUTHOR*(s)* Alan L. McWhorter		8. CONTRACT OR GRANT NUMBER*(s)* F19628-76-C-0002
9. PERFORMING ORGANIZATION NAME AND ADDRESS Lincoln Laboratory, M.I.T. P.O. Box 73 Lexington, MA 02173		10. PROGRAM ELEMENT, PROJECT, TASK AREA & WORK UNIT NUMBERS Program Element No. 65705F Project No. 649L
11. CONTROLLING OFFICE NAME AND ADDRESS Air Force Systems Command, USAF Andrews AFB Washington, DC 20331		12. REPORT DATE 15 August 1977
		13. NUMBER OF PAGES 68
14. MONITORING AGENCY NAME & ADDRESS *(if different from Controlling Office)* Electronic Systems Division Hanscom AFB Bedford, MA 01731		15. SECURITY CLASS. *(of this report)* Unclassified
		15a. DECLASSIFICATION DOWNGRADING SCHEDULE
16. DISTRIBUTION STATEMENT *(of this Report)* Approved for public release; distribution unlimited.		
17. DISTRIBUTION STATEMENT *(of the abstract entered in Block 20, if different from Report)*		
18. SUPPLEMENTARY NOTES None		
19. KEY WORDS *(Continue on reverse side if necessary and identify by block number)* solid state devices surface-wave technology imaging arrays quantum electronics photodiode devices infrared imaging materials research lasers surface-wave transducers microelectronics laser spectroscopy		

20. ABSTRACT *(Continue on reverse side if necessary and identify by block number)*

This report covers in detail the solid state research work of the Solid State Division at Lincoln Laboratory for the period 1 May through 31 July 1977. The topics covered are Solid State Device Research, Quantum Electronics, Materials Research, Microelectronics, and Surface-Wave Technology. Funding is primarily provided by the Air Force, with additional support provided by the Army, ARPA, NSF, and ERDA.